Tau differentially regulates the transport of early endosomes and lysosomes

Linda Balabanian[a], Dominique V. Lessard[b], Karthikeyan Swaminathan[a], Pamela Yaninska[c], Muriel Sébastien[a], Samuel Wang[a], Piper W. Stevens[a], Paul W. Wiseman [c], Christopher L. Berger[b], and Adam G. Hendricks [a,*]
[a]Departments of Bioengineering and [c]Chemistry and Physics, McGill University, Montreal, QC H3A 0E9, Canada;
[b]Department of Molecular Physiology and Biophysics, University of Vermont, Burlington, VT 05405

ABSTRACT Microtubule-associated proteins (MAPs) modulate the motility of kinesin and dynein along microtubules to control the transport of vesicles and organelles. The neuronal MAP tau inhibits kinesin-dependent transport. Phosphorylation of tau at Tyr-18 by fyn kinase results in weakened inhibition of kinesin-1. We examined the motility of early endosomes and lysosomes in cells expressing wild-type (WT) tau and phosphomimetic Y18E tau. We quantified the effects on motility as a function of the tau expression level. Lysosome motility is strongly inhibited by tau. Y18E tau preferentially inhibits lysosomes in the cell periphery, while centrally located lysosomes are less affected. Early endosomes are more sensitive to tau than lysosomes and are inhibited by both WT and Y18E tau. Our results show that different cargoes have disparate responses to tau, likely governed by the types of kinesin motors driving their transport. In support of this model, kinesin-1 and -3 are strongly inhibited by tau while kinesin-2 and dynein are less affected. In contrast to kinesin-1, we find that kinesin-3 is strongly inhibited by phosphorylated tau.

INTRODUCTION

A web of interactions between motor proteins, cargo adapters, and the cytoskeleton governs the transport of vesicles and organelles. The microtubule tracks control intracellular transport through micro-tubule-associated proteins (MAPs), tubulin posttranslational modifications, and the organization of the microtubule network. Teams of kinesin and dynein motor proteins associate with cargoes, which confer bidirectional motility and the flexibility to navigate obstacles and readily change microtubule tracks. Cytoplasmic dynein is responsible for retrograde transport in animal cells, while kinesins-1 (KIF5), -2 (KIF3), -3 (KIF1, KIF13, KIF16), and -4 (KIF21) drive antero-grade transport (Hirokawa and Takemura, 2005; Verhey and Gaertig, 2007; Hancock, 2014; Janke, 2014; Ghiretti et al., 2016; Balabanian et al., 2018).

The motility and positioning of lysosomes, driven by dynein and kinesins-1, -2, and -3, are crucial for robust proteostasis and immune responses (Pu et al., 2016). Kinesin-2 is required for the transport of late endosomes and lysosomes, but not early endosomes (Brown et al., 2005). In addition to kinesin-2, subpopulations of lysosomes are driven alternatively by kinesin-1 on juxtanuclear, acetylated microtubules and kinesin-3 (KIF1Bβ and KIF1A) on peripheral tyros-inated microtubules (Matsushita et al., 2004; Norris et al., 2014; Bentley et al., 2015; Guardia et al., 2016). Early endosomes, responsible for sorting endocytosed particles for recycling or lysosome-mediated degradation, are driven in the anterograde direction by kinesin-1, as well as members of the kinesin-3 family (KIF16B, KIF13A, KIF13B) (Hoepfner et al., 2005; Blatner et al., 2007; Delevoye et al., 2014; Bentley et al., 2015; Beaudet et al., 2022).

Recent studies from multiple groups indicate that kinesin-3 motors conduct transport of various cargoes on dynamic microtubules in more peripheral regions and presynaptic sites in neurons, whereas kinesin-1 acts on stable acetylated microtubules closer to the nucleus (Cai *et al.*, 2009; Konishi and Setou, 2009; Katrukha *et al.*, 2017; Tas *et al.*, 2017; Guedes-Dias *et al.*, 2019; Serra-Marques *et al.*, 2020).

The MAP tau stabilizes and bundles microtubules, acting as a spacer between neighboring microtubules in bundles (Kanai *et al.*, 1992; Scott *et al.*, 1992; Takemura *et al.*, 1992). Tau also inhibits the motility of motor proteins by blocking their interaction with microtubules (Vershinin *et al.*, 2007; Dixit *et al.*, 2008; McVicker *et al.*, 2011; Hoeprich *et al.*, 2014; Monroy *et al.*, 2018). Axonal microtubule bundles are heavily decorated with tau, yet robust intracellular transport in axons supports neuronal signaling and homeostasis (Kosik and Finch, 1987; Kanai and Hirokawa, 1995). Different types of kinesin are differentially affected by the presence of MAPs on the microtubule surface. Kinesin-1 does not readily circumvent tau obstacles on microtubules, whereas kinesin-2 and kinesin-8 navigate around tau (Shastry and Hancock, 2011; Hoeprich *et al.*, 2014; Guzik-Lendrum *et al.*, 2015; Malaby *et al.*, 2019).

Tau rapidly switches between states that statically bind or dynamically diffuse over the microtubule surface (Hinrichs *et al.*, 2012; McVicker *et al.*, 2014). The shortest tau isoform in the CNS, tau-3RS, binds more statically to the microtubule and most strongly inhibits kinesin in vitro (Vershinin *et al.*, 2007; Dixit *et al.*, 2008; McVicker *et al.*, 2011). Posttranslational modifications such as phosphorylation alter tau's conformation and surface charge, modulating its microtubule binding. Phosphomimetic tau (Y18E) has reduced affinity on reconstituted microtubules, increasing its diffusivity and consequently alleviating tau's inhibitory effect on purified kinesin-1 motors (Stern *et al.*, 2017). As such, the phosphorylation state of tau is an important factor in determining the processivity of motor motility.

More than 85 putative phosphorylation sites have been identified on tau, phosphorylated by multiple kinases including GSK3ß, AKT, MAPK, and Fyn (Sergeant *et al.*, 2008). Phosphorylation of tau at multiple sites is prevalent in tauopathies, and the aggregation of the hyperphosphorylated misfolded tau is correlated with worsening cognitive impairment (Ballatore *et al.*, 2007). The nonreceptor tyrosine kinase fyn phosphorylates tau at Y18 (Lee *et al.*, 2004), the last residue of the phosphatase-activating domain (PAD) of tau. Y18 phosphorylation prevents the PAD from activating the protein phosphatase 1 (PP1) and GSK-3 pathways, which otherwise inhibit anterograde fast axonal transport and mediate kinesin detachment from cargoes. Subsequently, Y18 phosphorylation of tau counteracts the inhibition by tau aggregates on anterograde fast axonal transport (Morfini *et al.*, 2004; LaPointe *et al.*, 2009; Kanaan *et al.*, 2011, 2012). Furthermore, PAD exposure and activity in tau aggregates found in Alzheimer's disease precede the phosphorylation at Y18 in aggregates during disease progression (Kanaan *et al.*, 2012). As such, fyn kinase–mediated phosphorylation at Y18 may confer a protective effect against tau inhibition of cargo transport.

Motivated by the apparent paradox between the observations that tau inhibits kinesin motility yet robust intracellular transport occurs along axonal microtubules decorated by tau, we asked whether tau phosphorylation at Y18 might modulate tau's inhibition of organelle transport. Further, we asked whether the effect of phosphorylation is different for cargoes driven by different types of kinesin motors (kinesin-1, -2, and -3), given the various sensitivities of motors to tau in vitro. We studied the localization and movement of lysosomes and early endosomes in cells exogenously expressing wild-type (WT) tau (shortest isoform tau-3RS) alone or with fyn kinase, or phosphomimetic tau (Y18E). We accounted for variable expression levels of tau in cells by quantifying tau intensity and measuring the response in the motility of cargoes as a function of the level of tau.

At low levels of tau expression, we found that phosphomimetic and phosphorylated tau partially rescue the inhibition of lysosome motility, compared with WT tau. Tau inhibition is specifically reduced for the subpopulation of lysosomes positioned in the perinuclear or juxtanuclear region, which are expected to be transported on stable acetylated microtubules primarily by kinesin-1 (Cai *et al.*, 2009; Katrukha *et al.*, 2017). In contrast, peripheral lysosomes, which localize on dynamic tyrosinated microtubules by kinesin-3 (Konishi and Setou, 2009; Norris *et al.*, 2014; Guardia *et al.*, 2016; Tas *et al.*, 2017; Guedes-Dias *et al.*, 2019; Serra-Marques *et al.*, 2020), were inhibited by phosphomimetic tau. WT tau inhibits both juxtanuclear and peripheral subpopulations of lysosomes similarly. Unlike lysosomes, early endosomes are inhibited by both phosphomimetic/phosphorylated tau and unphosphorylated (WT) tau. Using in vitro motility assays, we show that kinesin-3 motor proteins are inhibited by both phosphomimetic tau and WT tau on reconstituted, paclitaxel-stabilized microtubules. Previously, we showed that phosphomimetic tau, unlike WT tau, does not strongly inhibit kinesin-1 (Stern *et al.*, 2017). Microtubule bundling by tau is also expected to affect cargo transport. We observe that global rearrangements of the microtubule network occurred only with high levels of tau. Together, our results show that regulation of tau by Y18 phosphorylation differentially affects the displacement of specific cargoes.

RESULTS

Tau biases lysosome motility and localization to the perinuclear region

We examined the directionality of lysosomes in COS-7 fibroblast cells expressing varying levels of WT tau (wild type) or phosphomimetic tau (Y18E) (Figure 1, A and B). COS-7 cells do not endogenously express tau, such that the type of tau present can be tightly controlled. The flat morphology of COS-7 cells allows for high-resolution imaging using total internal reflection fluorescence (TIRF) microscopy (Supplemental Movie S1). Lysosomes are localized throughout the cell and concentrated in the perinuclear region, close to the microtubule-organizing center (MTOC) (Figure 1, A and B) (Pu *et al.*, 2016). Around half of all lysosomes are stationary in control cells (~51%), and the remaining lysosomes are evenly divided between active transport toward and away from the cell center (Figure 1, C and D).

We quantified the levels of tau expression in transfected cells by measuring tau-mApple intensity and normalizing to the background intensity outside of the cell. Tau enriches strongly on microtubules, with low cytosolic signal present in cells with low levels of tau (normalized tau intensity < 5) (Figure 1A, 1st row). Cells expressing medium levels (5 ≤ normalized tau intensity < 10) show a considerable cytosolic signal in the perinuclear region (Figure 1A, 2nd row), and finally high levels of tau expression (normalized tau intensity ≥ 10) exhibit cell-wide cytosolic signal (Figure 1A, 3rd row). We also coexpressed WT tau with fyn kinase (Supplemental Figure S1, A–F), which phosphorylates tau at Y18 (Supplemental Figure S2A) (Lee *et al.*, 2004), and found that fyn alone influences lysosome movement; thus we focused on directly comparing WT tau and tau Y18E. Lysosomes are more constrained to the perinuclear region (Figure 1A), and the percentage of stationary lysosomes accumulates with increasing tau expression, notably with medium and high levels of tau (Figure 1C; Supplemental Figure S1D), such that it distorts the analysis on the effects of tau on lysosome directionality in these cells (Supplemental
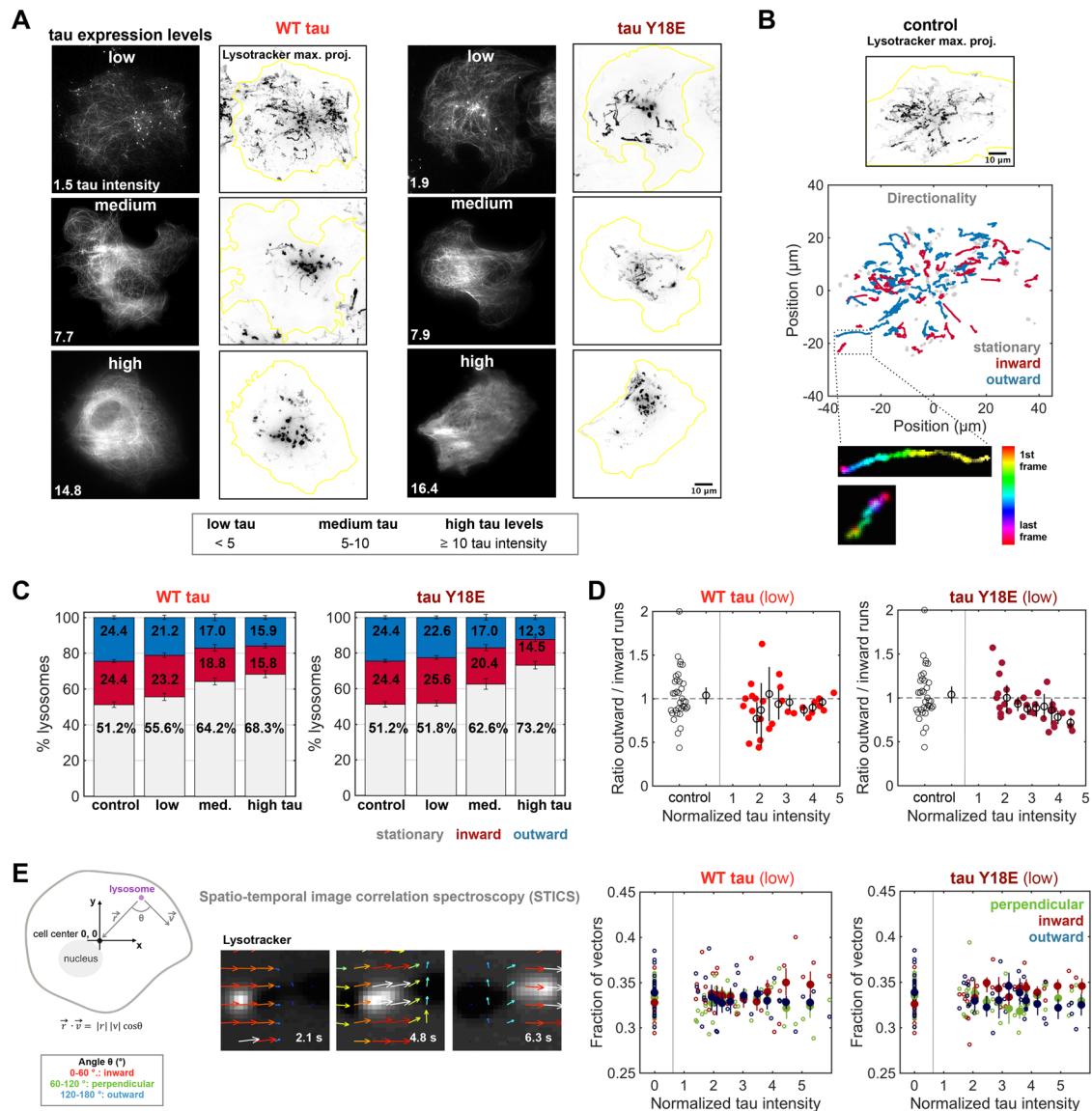
FIGURE 1: Tau biases lysosome motility toward the cell center. (A) Transient transfection results in variable tau-mApple expression levels. In cells expressing low levels (normalized tau intensity < 5), tau is enriched on microtubules and lysosomes are distributed throughout the cell, as seen on the maximum projections of lysosome movies. In cells expressing medium (5 ≤ normalized tau intensity < 10) and high (normalized tau intensity ≥ 10) levels of tau, tau is localized both along microtubules and in the cytosol. Lysosomes are more constrained to the perinuclear region in these cells. (B) The maximum projection image shows that lysosomes exhibit robust motility along microtubules in a control cell (with no tau expression). The net directionality of lysosome trajectories, tracked with TrackMate (Tinevez *et al.*, 2017), was categorized as inward (toward cell center) or outward (toward the cell periphery) for motile lysosomes (with radius of gyration Rg ≥ 0.5 μm) or as stationary (Rg < 0.5 μm). (C) The fraction of stationary lysosomes increases with the level of tau expression (mean ± SEM). (D) The fractions of inward and outward trajectories are approximately equal for motile lysosomes in control cells. The ratio of the number of outward to inward indicates that WT and Y18E tau reduce the fraction of outward movement. Small symbols indicate single cells, large symbols indicate the means± 95% CIs (error bars) calculated using bootstrapping. (E) STICS was used to calculate velocity fields of the lysosome movement. θ is defined as the angle between the velocity (*v*) vector and the vector (r) pointing from the lysosome to the cell center (0, 0). An angle of 0—60° indicates inward movement (toward cell center), 60–120° indicates perpendicular movement with respect to the cell center (depicted on the schematic), and 120–180° represents outward motion. Middle panels show the velocity vector field calculated using STICS. At right, the fractions of lysosome trajectories moving inward, outward, or perpendicular with respect to the cell center (for each cell) show that lysosomes move inward more often in cells expressing low levels of WT tau or Y18E tau, relative to control cells (small symbols: single cell; large symbols: mean± 95% CIs calculated using bootstrapping). Both the tracking-based directionality analysis (in C, D) and the STICS analysis (in E) demonstrate that lysosome motility is biased inward in response to tau. The plots for the data sets showing the cells over the whole range of tau expression levels (low, medium, high) are found in Supplemental Figure S1, D and E. (Control: *n* = 35 cells in C and D and 33 in E; WT tau: 71; Y18E tau: 83 cells.)

Figure S1, D and E). Low levels of tau in cells are comparable to endogenous tau levels in neuronal axons (Supplemental Figure S2, A–C) (Black et al., 1996; Xia et al., 2016). Consequently, we focus our analysis to cells expressing low levels of WT tau and phosphomimetic Y18E tau. We also performed three-dimensional (3D) structured illumination microscopy (SIM) imaging to assess whether the changes in lysosome localization we observe near the cell cortex using TIRF are representative of lysosome positioning throughout the volume of the cell. We find that, similar to that observed in TIRF images, Y18E tau reduces the number of lysosomes in the periphery more strongly compared with WT tau (Supplemental Figure S3, A and B).

Microtubules exhibit robust dynamics in cells expressing low levels of WT tau or Y18E tau (Supplemental Figure S4A). However, microtubule organization is altered dramatically with high levels of tau expression (Supplemental Figure S4). Tau binds along the length of microtubules (Supplemental Figure S4B) (Samsonov et al., 2004) and bundles microtubules, acting as a spacer between adjacent microtubules (Chen et al., 1992; Kanai et al., 1992; Scott et al., 1992; Takemura et al., 1992). We studied peripheral microtubule density and bundling in cells to distinguish the effect of tau on cargo transport from its indirect influence on cargo motion through remodeling of the microtubule network (Supplemental Figure S4). High levels of tau dramatically rearrange the microtubule network into thick microtubules bundles in a ring-shaped array in the periphery (Supplemental Figure S4, C–G) (Yu et al., 2016). Lysosomes are trapped within the bundled microtubule rings, and some lysosomes are seen circling around the interior edges (Supplemental Figure S4H). Fyn kinase overexpression alone also increases peripheral microtubule density (Supplemental Figure S4, C, D, and G). At low levels of WT tau or tau Y18E expression, most cells retained a radial organization of microtubules similar to that of control (Supplemental Figure S4, D–F). Overall, lysosome directionality (Figure 1), motility (Figures 2 and 3) and localization (Figure 3) are unlikely to be affected by tau's effect on microtubule organization at low tau levels, as extreme reconfigurations of the microtubule network occur with high amounts of tau.

Both low levels of WT tau and phosphomimetic Y18E tau cause an increase of lysosome motility toward the cell center, as shown by tracking analysis (Figure 1D, 95% confidence intervals [CIs]). Single-particle tracking can be challenging in situations where particles are clustered. Thus, we applied spatiotemporal image correlation spectroscopy (STICS), which generates vector fields based on the correlation of pixel intensities over a range of spatial and temporal scales (Figure 1E; Supplemental Figure S1E). STICS also demonstrates that tau results in an inward bias in lysosome motility (Figure 1E, 95% CIs). Both single-particle tracking and correlation analysis show that tau biases lysosome motility toward the cell center, in agreement with in vitro motility assays of isolated phagosomes (Chaudhary et al., 2018), and leads to the enrichment of stationary lysosomes in the perinuclear region with increasing levels of tau.

Phosphorylation at Y18 reduces tau-mediated inhibition of lysosome transport

Using high-resolution tracking, we analyzed the motility of lysosomes stained with Lysotracker Deep Red in live cells (Figure 2A). Lysotracker enriches in acidic compartments including endolysosomes, autolysosomes, and phagolysosomes. We measured the mean-squared displacement (MSD) of lysosome trajectories and calculated the slope (α value) to determine the type of motion ($\alpha < 1$ for confined, $\alpha = 1$ for diffusive, $\alpha > 1$ for directed motion) (Tarantino et al., 2014). We also calculated the radius of gyration (Rg) of each trajectory as a measure of the distances traveled by

the cargoes. Each trajectory is weighted equally in the calculation of the mean Rg, while the MSD weighs each delay period equally such that long trajectories are weighted more heavily than short trajectories. MSD analysis shows that low levels of WT tau constrain lysosomal motion, while lysosome processivity in cells expressing phosphomimetic Y18E tau remains similar to that in control cells (Figure 2B), in agreement with Rg analysis of trajectories (Figure 2C). The processivity (α) of lysosomal trajectories decreases in cells expressing WT tau compared with control (one-way analysis of variance [ANOVA], Tukey's test, $p < 0.0001$) and compared with tau Y18E ($p < 0.0001$), while the distributions remain similar for control cells and tau Y18E cells ($p = 0.32$) (Figure 2D). Overall, the motility of lysosomes decreases with increasing levels of tau (Figure 2, E and F; Supplemental Figure S5, D–F, 95% CIs). WT tau reduces processivity (Figure 2E) and distances traveled by lysosomes (Figure 2F), even at low levels of tau expression. Interestingly, at low levels, phosphomimetic Y18E tau does not decrease the processivity and displacement of lysosomes, which remain similar to those of control (Figure 2, E and F, 95% CIs).

Fyn kinase decreases lysosomal displacement and processivity. However, coexpression of fyn and low levels of WT tau did not lead to a further reduction, suggesting that phosphorylated tau does not strongly inhibit lysosome movement (Supplemental Figure S5, A–D). The α distribution for cells expressing fyn alone (two-way ANOVA, $p = 0.0008$) or with WT tau also demonstrates that phosphorylated tau (WT tau + fyn) does not behave like WT tau (interaction tau and fyn: $p = 0.013$) (Supplemental Figure S5B). Together, these results show that low levels of phosphomimetic or phosphorylated tau at Y18 do not strongly inhibit lysosome motility, compared with nonphosphorylated (WT) tau.

We examined the speed and pausing behavior of lysosomes (Supplemental Figure S5, G–I). Lysosome trajectories typically consist of motile and paused segments (Supplemental Figure S5, G and H). The average speed of lysosomes when excluding paused segments does not vary considerably with increasing levels of tau expression (Supplemental Figure S5I). Comparatively, the average speed when including detected paused segments of trajectories decreases to a greater extent, as the percentage of time spent pausing within trajectories increases with tau (Supplemental Figure S5I). At low levels of expression, lysosomes in phosphomimetic tau Y18E–expressing cells exhibited a lower average speed and higher percentage of time spent pausing relative to WT tau (Supplemental Figure S5I). Taken together with the finding that lysosomes travel longer distances in the presence of phosphomimetic tau, lysosomes often briefly pause and then continue to move rather than stopping or dissociating from the microtubule.

Phosphomimetic tau (Y18E) inhibits the motility of peripheral lysosomes but not juxtanuclear lysosomes

The distribution of both stationary lysosomes and lysosomes moving longer distances is uniform in perinuclear, juxtanuclear, and peripheral regions of control cells and cells expressing low levels of WT tau (Figure 3A). In contrast, lysosomes with long runs ($Rg \geq 1$ μm) are concentrated in the juxtanuclear region of tau Y18E–expressing cells (Figure 3A). Fewer lysosomes localized in the periphery with phosphomimetic Y18E tau (Supplemental Figure S6A). Stationary lysosomes or lysosomes with short runs are still found in the periphery of some cells (Figure 3A, top panels) and nearly absent altogether in others (Figure 3A, bottom panels, orange arrows). With phosphomimetic Y18E tau, cells that have fewer peripheral lysosomes (Figure 3A bottom panels; Supplemental Figure S6B) show a
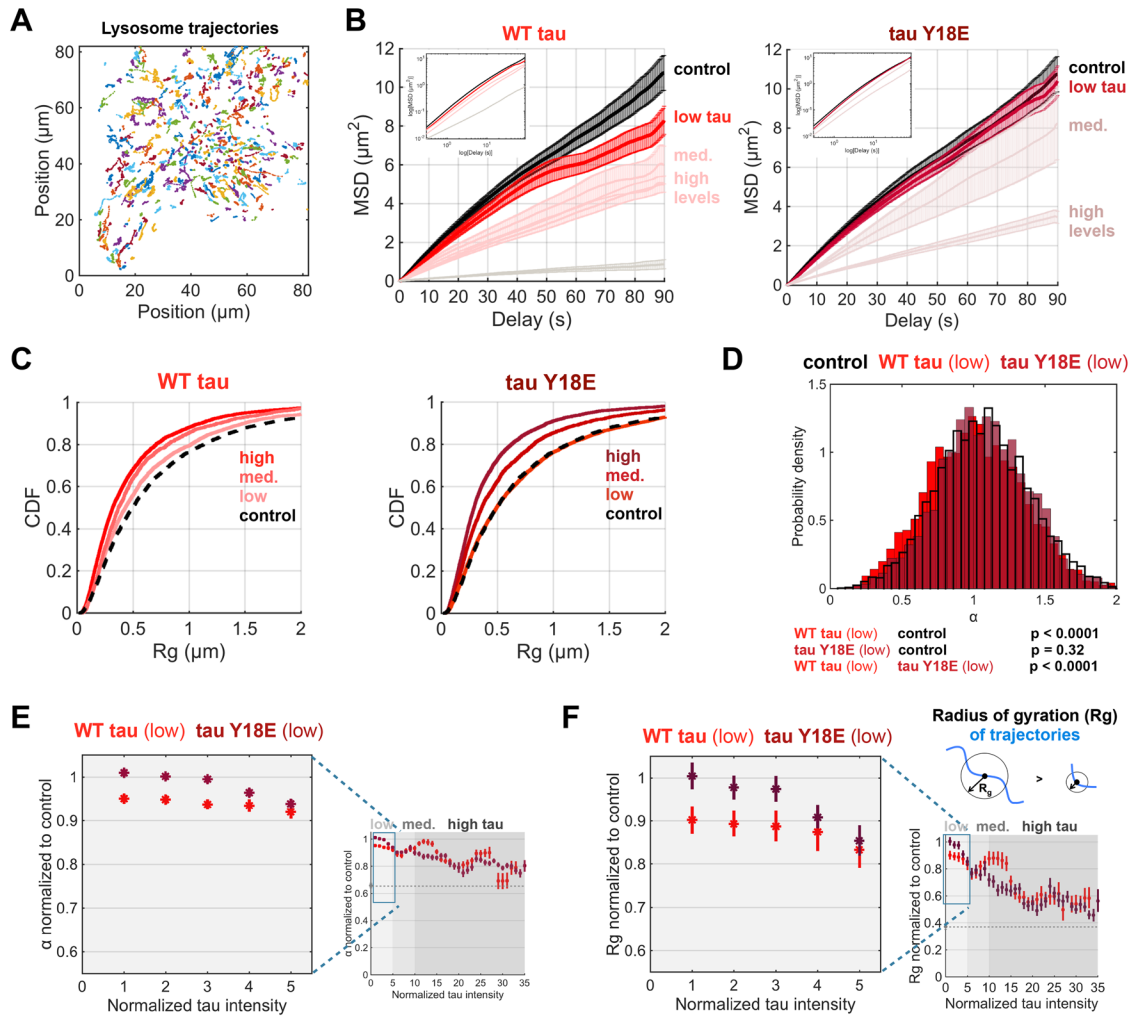
FIGURE 2: Phosphorylation of tau at Y18 relieves the inhibition of lysosome motility. (A) Lysosomes were imaged for 90 s and tracked using TrackMate in ImageJ (Tinevez *et al.*, 2017). Lysosome trajectories from a control cell are shown here. (B) The MSDs of lysosomes in cells expressing low levels of tau Y18E are similar to that of control, whereas low levels of WT tau inhibit lysosome motility (mean ± SEM). For comparison, treatment with 10 µM nocadozole abolishes microtubule-dependent vesicle transport (gray line, *n* = 825 trajectories, nine cells). Log-log plots are shown as insets. (C) The cumulative distribution function (CDF) of the *R*g of trajectories demonstrates a reduction of motility with higher tau levels, while at low levels, Y18E tau inhibition of lysosome motility is small (95% bootstrap CIs: control [0.73, 0.77], WT tau (low) [0.65, 0.70], Y18E tau (low) [0.73, 0.78] µm). (D) The slope of the MSD (α) indicates the proportion of stationary (α = 0), diffusive (α = 1), and processive (α = 2) motility. α values for cells expressing low levels of WT tau are reduced compared with control and tau Y18E (one-way ANOVA, Tukey's test, *p* < 0.0001). Low levels of tau Y18E do not decrease lysosome processivity compared with control (*p* = 0.32). Ninety-five percent bootstrap CIs were also calculated (1000 iterations): control [1.05, 1.07], WT tau (low) [1.00, 1.02], Y18E tau (low) [1.06, 1.08]. (E) Sliding means of the α values were calculated as a function of tau intensity for trajectories in cells expressing low levels of WT tau or tau Y18E (left plot). Processivity (α) decreases progressively with tau intensity (right plot, mean± 95% CIs). (Control: *n* = 4882 trajectories; fyn: 2149; WT tau: 7910; Y18E tau: 9970; WT tau + fyn: 4644 trajectories.) (F) The *R*g is an indicator of the mean distance traveled in a trajectory (see *Materials and Methods*), where a circle with radius *R*g contains half of the spots of the trajectory. Lysosome displacement is inhibited less by phosphomimetic Y18E tau than WT tau (left plot). The displacement of lysosomes decreases with increasing tau intensity over the wider range of tau intensities (right plot, mean± 95% CIs). Control: *n* = 5408 trajectories, from *n* = 35 cells, over 20 experiments; WT tau: 9024 traj., 73 cells, over 14 experiments; Y18E tau: 11105 trajectories, 83 cells, over five experiments. This analysis uses the same data set as in Figure 1. The α and *R*g of lysosome trajectories in cells treated with 10 µM nocodazole (mean and 95% CI at *x* = 0 and with a line) are shown on the right plot of E and F (*n* = 825 trajectories for α and 985 for *R*g, nine cells).

higher mean for lysosome displacement (Spearman's correlation coefficient ρ = –0.41, *p* = 0.02), while no correlation is found for control and WT tau–expressing cells (Supplemental Figure S6C). Phosphomimetic Y18E tau expression, unlike WT tau expression, is differentially affecting the motility of lysosomes positioned centrally or peripherally.

Lysosome trajectories were projected on polar plots to measure their distance from the cell center, and localization was categorized into three subcellular regions: peripheral, juxtanuclear, and perinuclear (Figure 3B; see *Materials and Methods*). Cells expressing even low levels of phosphomimetic Y18E tau show a significant loss of outward- and inward-moving lysosomes in the periphery compared
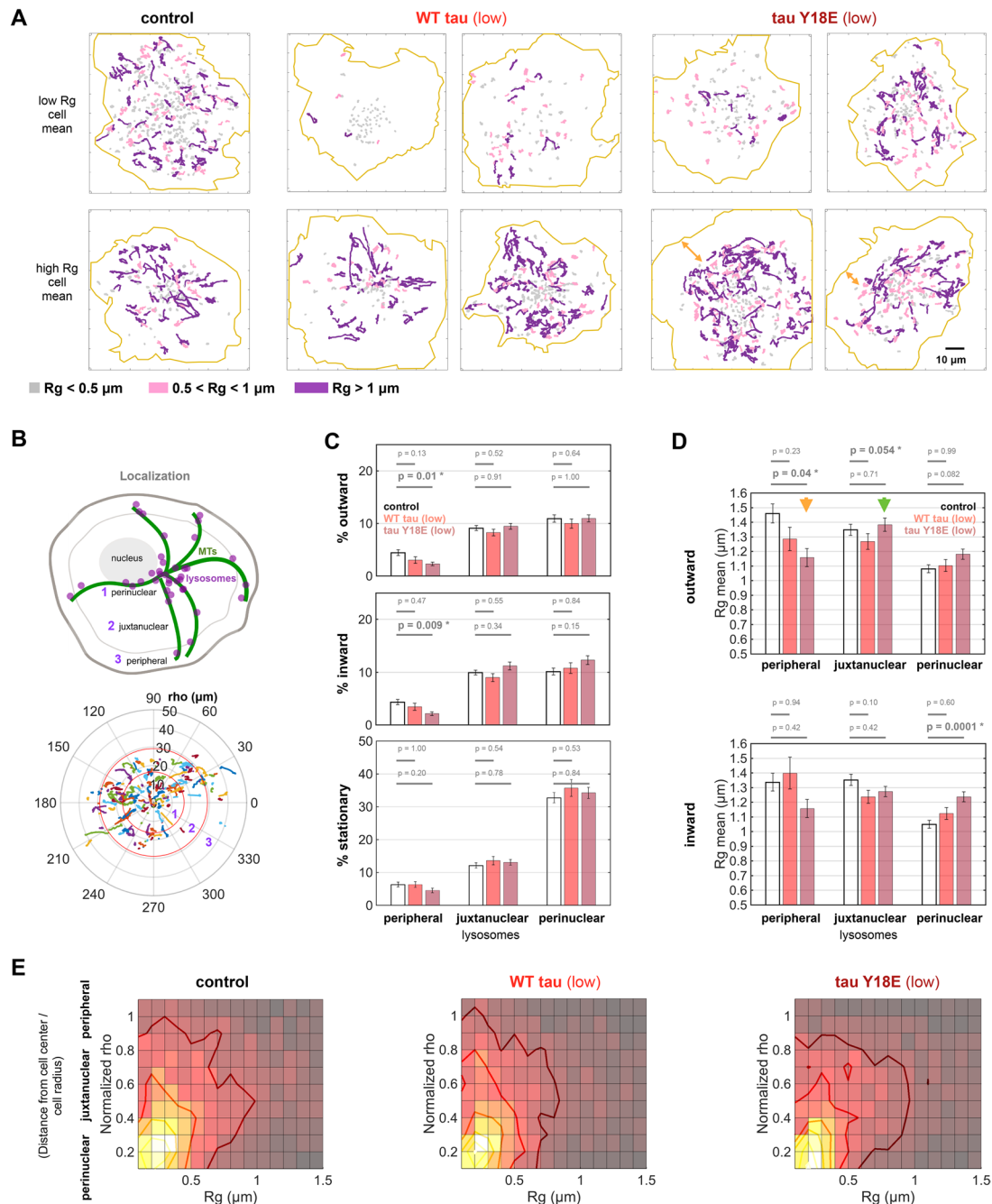
FIGURE 3: Phosphomimetic tau Y18E inhibits the motility of lysosomes in the cell periphery. (A) Stationary (gray), short (magenta), and long (purple) trajectories (over 90 s movies) are distributed throughout the control cells. WT tau expression results in fewer long trajectories in all regions of the cell. In contrast, Y18E tau expression preferentially inhibits long trajectories in the cell periphery and often precludes lysosomes in this region (orange arrows). For comparison, representative images for cells with low and high average lysosome displacement (*R*g) are shown. (B) Rho is defined as the mean distance of each trajectory from the cell center normalized to the average radius of the cell. Lysosomes were categorized as perinuclear (rho < 0.5), juxtanuclear (0.5 ≤ rho < 0.85), and peripheral (rho ≥ 0.85). (C) The percentage of inward-directed, outward-directed, and stationary lysosomes in different regions of the cell (mean ± SEM) indicates that the proportion of moving lysosomes in both the inward and outward directions is significantly reduced in the periphery of cells expressing Y18E tau. (D) The mean *R*g (±SEM) of motile lysosomes (*R*g > 0.5 µm) moving in the outward direction (top panels) or inward direction (bottom panels) is shown for each region of the cell (peripheral, juxtanuclear, or perinuclear localization). Juxtanuclear lysosomes maintain outward displacement similar to that of control in the presence of Y18E tau (green arrow), while peripheral lysosomes are inhibited by tau Y18E (orange arrow). *p* values from one-way ANOVA and Tukey's test are shown on bar charts for low levels of WT tau or Y18E tau expression compared with control. (E) The distribution of lysosomes with respect to their *R*g and localization. The distribution of moving lysosomes (*R*g ≥ 0.5 µm) in Y18E tau–expressing cells is concentrated in the juxtanuclear region, while moving lysosomes are more evenly distributed across regions in control and WT tau–expressing cells. Lines show contours of the 2D distribution. (Control: *n* = 35 cells, WT tau [low]: 29 cells; Y18E tau [low]: 31 cells.) This analysis uses the same data set as in Figure 1.

with control (one-way ANOVA, Tukey's test, $p = 0.01$ and 0.009, respectively), which is not seen with low levels of WT tau (Figure 3C). The loss of peripheral lysosomes occurs more prominently with tau Y18E than with unphosphorylated (WT) tau (Figure 3, A and C; Supplemental Figure S6A).

Overall, the localization of lysosomes in the periphery and the motility of lysosomes drop gradually with increasing tau levels, consistent with inhibition of kinesin-dependent transport toward distal regions of the cell (Supplemental Figure S6, D and E). Previous studies suggest that centrally localized lysosomes are to a large extent driven by kinesin-1 on acetylated microtubules, whereas peripheral lysosomes are transported primarily by kinesin-3 on tyrosinated microtubules (Guardia *et al.*, 2016; Tas *et al.*, 2017; Serra-Marques *et al.*, 2020). As such, we hypothesized that juxtanuclear and peripheral lysosomes would be affected to different extents by tau. In cells expressing low levels of WT tau, lysosomes positioned peripherally or in the juxtanuclear region are inhibited (log-normalization, one-way ANOVA, Tukey's test, $p = 0.054$) and exhibit similar displacement in the outward direction (Figure 3D). However, in cells expressing low levels of phosphomimetic Y18E tau, juxtanuclear lysosomes travel distances similar to those of control (green arrow, $p = 0.71$), while motility is reduced for peripheral lysosomes (Figure 3D, orange arrow, $p = 0.04$). As expected, low levels of WT tau did not inhibit inward-moving peripheral lysosomes (Figure 3D, $p = 0.94$), as the dynein motors responsible for inward transport are less sensitive to tau (Dixit *et al.*, 2008; Vershinin *et al.*, 2008; Chaudhary *et al.*, 2018). Y18E tau increases the displacement of lysosomes in the perinuclear region (Figure 3D, $p = 0.0001$), suggesting that the motors that transport lysosomes near the cell center are not inhibited by Y18E tau. STICS analysis reveals an inward bias in the movement of remaining lysosomes in the periphery (Supplemental Figure S6F), which could lead to the overall loss of peripheral lysosomes over time with Y18E tau, coincidentally where acetylated microtubules are scarce (Supplemental Figure S6G). The persistent motility of lysosomes in Y18E tau cells in central regions corresponds with the regions enriched in acetylated microtubules (Supplemental Figure S6G).

Fyn kinase increases the fraction of stationary lysosomes in the periphery and juxtanuclear region (Supplemental Figure S6, A and D, two-way ANOVA, $p = 0.013$ and 0.0028, respectively) and reduces the fraction of perinuclear-moving lysosomes (Supplemental Figure S6D, $p = 0.0013$ and 0.0016 for outward- and inward-moving lysosomes, respectively). Fyn is a nonreceptor tyrosine kinase associated with membrane components and involved in many signaling pathways controlling morphological differentiation and cytoskeletal rearrangements near the membrane for process outgrowth (Klein *et al.*, 2002; White and Kramer-Albers, 2014), which could explain why microtubule density in the periphery is also altered with fyn overexpression (Supplemental Figure S4, C–E and G) and why lysosomes are more enriched in the periphery of fyn-transfected cells (Supplemental Figure S6, A and D). Most interestingly, we show that motile lysosomes ($R_g \geq 0.5$ μm) are more enriched in the juxtanuclear region of cells expressing low levels of phosphomimetic Y18E tau compared with the more dispersed distribution of lysosomes found in control cells and cells expressing low levels of WT tau (Figure 3E).

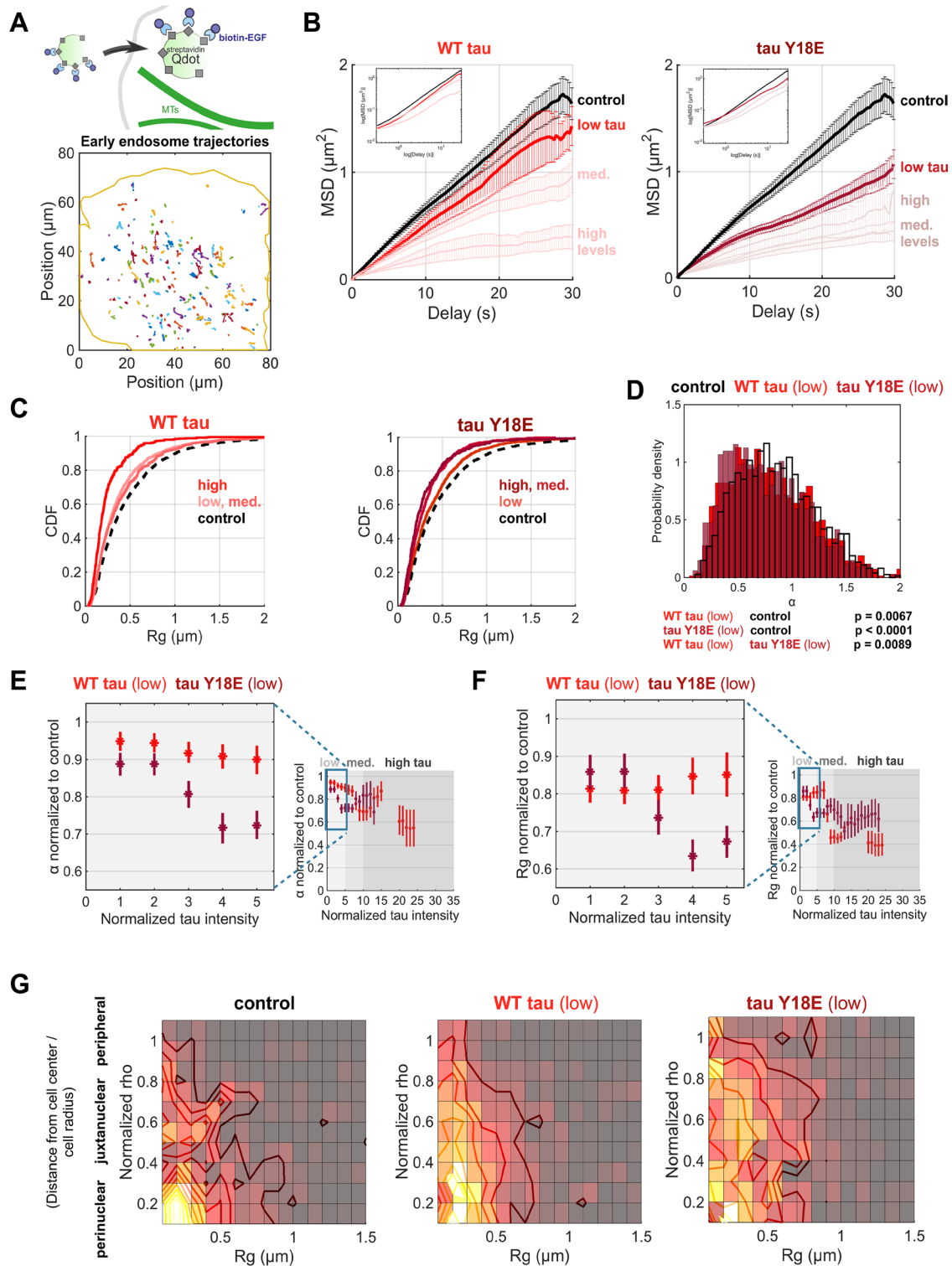### Early endosome motility is inhibited by both WT tau and Y18 phosphorylated tau

The observation that tau has different effects on subpopulations of lysosomes positioned centrally or peripherally suggested that tau phosphorylation might have various effects on other organelles.

Streptavidin quantum dots (Qdots) coated with biotinylated epidermal growth factor (EGF) were endocytosed into COS-7 fibroblast cells to label early endosomes (Zajac *et al.*, 2013) (Figure 4A). Qdot-containing early endosomes exhibit shorter bursts of directed motion (Figure 4A; Supplemental Figure S7, A and B; Supplemental Movie S2) compared with lysosomes, which are more processive and bidirectional (Figure 2A). Fyn kinase overexpression strongly inhibits early endosome motion with or without tau (Supplemental Figure S7, A–H). Directed motion is still observed with low levels of WT tau or phosphomimetic Y18E tau, but is nearly absent for cells with medium and high levels of tau (Supplemental Figure S7, B and F–H).

MSD analysis shows that low levels of both WT tau and Y18E tau inhibit early endosome motility and that phosphomimetic Y18E tau is more inhibitory to these cargoes than WT tau (Figure 4B), in agreement with the R_g distributions of early endosome trajectories (Figure 4C). The processivity (α) of trajectories in cells expressing low levels of WT tau and phosphomimetic Y18E tau is reduced relative to that of control (one-way ANOVA, Tukey's test, $p = 0.0067$ and $p < 0.0001$, respectively) (Figure 4D). Analysis of trajectories of Qdot-containing early endosomes revealed that WT tau and phosphomimetic tau inhibit both the processivity (Figure 4E) and displacement (Figure 4F, 95% CIs) of early endosomes. STICS analysis shows that the fraction of outward movement of early endosomes is reduced in Y18E tau–expressing cells (Supplemental Figure S7I). The localization of early endosomes, which lacks a distinct distribution pattern compared with that of lysosomes, does not differ in cells expressing WT and Y18E tau (Figure 4G). In addition, early endosomes are more sensitive to tau compared with lysosomes as their displacement is highly inhibited at even medium levels of tau, while lysosomes reached that level of inhibition with higher amounts of tau (Figures 2, E and F, and 4, E and F). In contrast to lysosomes, early endosome motility is strongly inhibited by phosphomimetic Y18E tau.

WT tau and phosphomimetic tau at Y18 inhibit kinesin-3 in vitro

We next asked whether the variable responses of different cargoes to tau might be explained by the sensitivity of different kinesin motors to tau. Peripheral lysosomes and early endosomes show reduced motility in the presence of low levels of phosphomimetic Y18E tau, while juxtanuclear lysosomes demonstrate motility similar to that of control (Figures 3 and 4). Kinesin-3 contributes to the motility of the cargoes that are sensitive to Y18E tau (Hoepfner *et al.*, 2005; Bentley *et al.*, 2015; Guardia *et al.*, 2016), leading to the hypothesis that kinesin-3, unlike kinesin-1, is inhibited by phosphomimetic tau. To investigate the effect of phosphomimetic tau on kinesin-3 directly, we performed kinesin-3 (KIF1A) motility assays on reconstituted microtubules in vitro (Figure 5A). KIF1A run lengths dropped to nearly half of that of control with 200 nM WT tau (equivalent to a 1:5 tau:tubulin ratio) (one-way ANOVA, Tukey's test, $p < 0.0001$) and were reduced even further with phosphomimetic Y18E tau (Figure 5B, $p < 0.0001$). The overall speed of the motor protein is relatively higher with WT tau compared with control due to reduced interrun pausing (Figure 5 A and C, $p = 0.0002$). We previously showed that kinesin-1 run lengths are also strongly reduced by WT tau but that the inhibition was relieved with phosphomimetic Y18E tau (Stern *et al.*, 2017) (Figure 5D). Thus, kinesin-1 and kinesin-3 are differentially affected by tau phosphorylation at Y18, where phosphorylation reduces the inhibition of kinesin-1 motility but enhances the inhibition of kinesin-3 motility (Figure 5D).

FIGURE 4: WT and phosphomimetic tau strongly inhibit early endosome motility. (A) EGF-coated Qdots were used to image early endosomes (<1 h postinternalization) and tracked using TrackMate (Tinevez *et al.*, 2017). Early endosomes exhibit short processive runs (control cell shown here). (B) MSD analysis shows that low levels of both WT tau and Y18E tau inhibit early endosome motility. In contrast to that of lysosomes, early endosome motility is more strongly inhibited by Y18E tau than WT tau. Log-log MSD plots are shown as insets. (C) The CDF of the R_g of early endosomes is shown for cells expressing low, medium, and high levels of WT tau and Y18E tau compared with control (95% bootstrap CI: control [0.46, 0.51], WT tau [low] [0.38, 0.41], Y18E tau [low] [0.40, 0.44] μm). (D) The distribution of MSD α values indicates that WT and Y18E tau reduce early endosome processivity (one-way ANOVA, Tukey's test). Ninety-five percent bootstrap CI: control [0.84, 0.87], WT tau [low] [0.79, 0.83], Y18E tau [low] [0.73, 0.78]. (E) The MSD α (mean± 95% CIs) of early endosomes, normalized to the mean α of control trajectories, shows inhibition of early endosome processivity with low levels of WT tau and Y18E tau. Control: $n = 1394$ trajectories; fyn: 148; WT tau: 1653; Y18E tau: 1185;
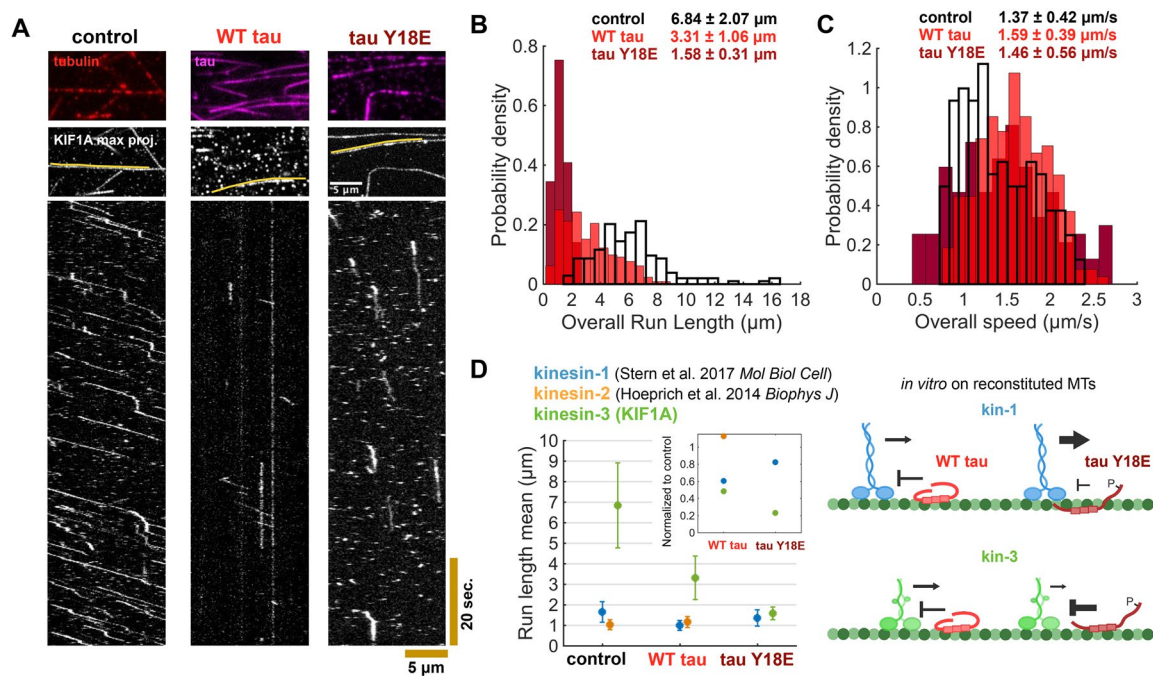
FIGURE 5: Kinesin-3 (KIF1A) is inhibited by WT and phosphomimetic Y18E tau in vitro. (A) Single-molecule motility assays (Supplemental Movie S3) on reconstituted microtubules indicate that KIF1A(1-393)-LZ-3xmCitrine processivity is strongly reduced in the presence of WT and Y18E tau, compared with control (no tau), as seen on kymographs. (B) WT tau and tau Y18E decrease KIF1A run lengths (one-way ANOVA, Tukey's test, $p < 0.0001$), with Y18E tau causing a greater inhibition than WT tau ($p < 0.0001$). (C) KIF1A exhibits fewer interrun pauses (A) in the presence of WT tau, resulting in higher velocities ($p = 0.0002$). Y18E tau's effect on KIF1A's speed is not significant ($p = 0.35$). (Control: 144 trajectories, WT tau: 212, Y18E tau: 153 trajectories.) (D) Tau phosphorylation has differential effects on kinesin-1 (Stern *et al.*, 2017) and kinesin-3 (as seen in A-C) on reconstituted microtubules (MTs) in vitro. Experimental conditions were similar (kinesin-1 and kinesin-2: 10 mM PIPES, 50 mM potassium acetate, 4 mM magnesium acetate; kinesin-3: 12 mm PIPES, 1 mm MgCl$_2$; All: supplemented with 1 mM EGTA, 10 mM DTT, and an oxygen scavenger system (5.8 mg/ml glucose, 0.045 mg/ml catalase, and 0.067 mg/ml glucose oxidase). The inset show the run length mean values normalized to that of control. While tau-mediated inhibition of kinesin-1 is reduced by phosphomimetic Y18E tau, the inhibition on kinesin-3 by tau increases with Y18E tau, as depicted on the schematic.

We next examined the interaction between tau and kinesin-3 (KIF1A) in living cells (Figure 6). In cells expressing KIF1A alone (Figure 6A) or with low tau expression, KIF1A localizes dynamically on peripheral microtubules (Figure 6B) (Hammond *et al.*, 2009). When tau is present, KIF1A is enriched in stable protrusions. KIF1A is also enriched on curved sections of microtubules in cells coexpressing tau (Figure 6C, insets), reminiscent of tau enrichment on curved microtubules (Samsonov *et al.*, 2004; Balabanian *et al.*, 2017). Interestingly, we found that when KIF1A and tau (WT tau or tau Y18E) were cotransfected in cells, tau is excluded from binding KIF1A-enriched microtubules in the periphery (Figure 6C), whereas tau binds all microtubules when expressed alone (Supplemental Figure S4, A and B). These results support the idea that KIF1A and tau compete for access to the microtubule lattice (Lessard *et al.*, 2019) and that kinesin-3 localization and motility are sensitive to both WT and Y18E tau.

DISCUSSION

Intracellular cargoes navigate a complex cytoskeleton to their specific destinations in the cell. Tight control of vesicular trafficking is required to maintain signaling and degradative pathways. By organizing microtubules and altering the interaction between motor proteins and their microtubule tracks, microtubule-associated proteins are a key component of the regulatory network. Through high-resolution tracking and spatiotemporal motility analysis of vesicles, we show that tau differentially regulates early endosomes and lysosomes. Early endosome motility is inhibited by even low levels of tau, while lysosome motility is less sensitive. Early endosomes are inhibited by both unphosphorylated (WT) tau and phosphomimetic (Y18E) tau, while lysosome motility is not strongly affected by phosphomimetic tau. Taken together, our results indicate that tau differentially affects the motility of early endosomes and lysosomes.

When cells overexpressed WT tau, the processivity of early endosomes and lysosomes is reduced, with fewer cargoes

---

WT tau + fyn: 338 trajectories. (F) The R_g of early endosome trajectories similarly shows early endosome inhibition by both WT tau and Y18E tau. Thus, Y18 phosphorylation of tau does not relieve tau-mediated inhibition of early endosomes. (Control: $n = 1946$ trajectories, from 28 cells, over 19 experiments; WT tau: 2783 traj., 84 cells, over 15 experiments; Y18E tau: 2193 trajectories, 53 cells, over six experiments.) (G) The distribution of early endosomes is shown with respect to their localization from cell center and the R_g of trajectories. (Control: $n = 522$ trajectories, from 10 cells; WT tau [low]: 813 traj., 17 cells; Y18E tau: 596 trajectories, 15 cells.)
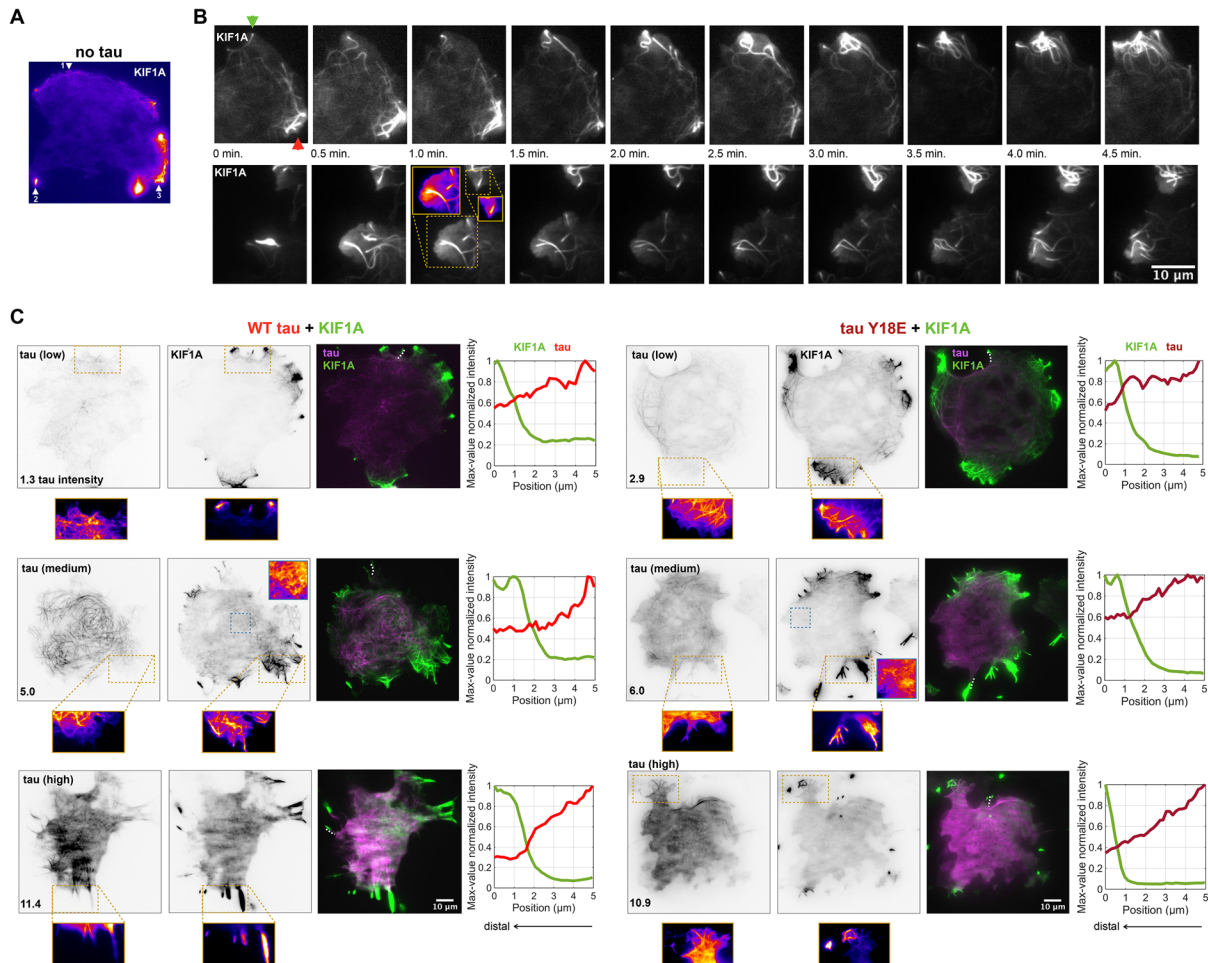
FIGURE 6: KIF1A localizes to peripheral microtubules and excludes tau binding. (A) In cells transfected with KIF1A (KIF1A(1-393)-LZ-3xmCitrine), KIF1A dynamically localizes at microtubule tips (arrow 1), accumulates on microtubules in protrusions (arrow 2), and binds along the length of peripheral dynamic microtubules (arrow 3) (Supplemental Movie S4). (B) The dynamic localization of KIF1A is also observed in cells expressing low levels of tau (normalized WT tau intensity here is 1.2 for top panels, and normalized Y18E tau intensity is 1.7 for bottom panels), and microtubules exhibit polymerization dynamics. In the example here, KIF1A binds a growing microtubule tip, which probes close to the membrane (green arrow), and the KIF1A intensity increases at the microtubule tip. More KIF1A-bound microtubule ends grow and converge into that area with time. KIF1A intensity decreases gradually below (red arrow). KIF1A intensities also change in cytosolic areas around KIF1A-enriched dynamic microtubules (insets), while the membrane protrudes outward. (C) KIF1A localization in the periphery excludes WT and phosphomimetic tau microtubule binding. The merged images show little overlap between tau and KIF1A. Intensity values of KIF1A and tau normalized to their respective maximum-intensity value over the ROIs (white dotted line on merged images) show that tau intensity decreases as the KIF1A signal rises. Additionally, we observe that KIF1A is enriched on curved microtubules in cells coexpressing tau (insets). (KIF1A without tau: 6, WT tau + KIF1A: 40, Y18E tau + KIF1A: 45 observed cells.)

undergoing directed motion while lysosomes are less sensitive to phosphomimetic tau. In agreement, phosphomimetic mutations of the longest tau isoform in the CNS at 18 serine/threonine sites, many of which are normally phosphorylated by GSK-3 kinase, did not significantly affect the kinetics of moving tau particles driven by motor proteins, but rather increased the number of motile particles in axons, compared with WT tau (Rodriguez-Martin *et al.*, 2013). Our results also indicate that unphosphorylated (WT) tau reduces the probability of cargoes to undertake directed motion, whereas phosphorylation of tau relieves this inhibition for specific cargoes. Phosphorylation is thought to reduce tau inhibition on cargo transport by introducing negative charges on tau, which might attract the positively charged motor domains of kinesin (Tarhan *et al.*, 2013). Additional negative charges on tau might also reduce the

affinity of tau to the microtubule surface, increasing the diffusivity of tau and, in turn, decreasing the probability of hindering kinesin's microtubule attachment (Rodriguez-Martin *et al.*, 2013; Stern *et al.*, 2017). The negative charge at Y18 also possibly alters the conformation of tau to favor the dynamic microtubule binding state, reducing the likelihood of tau acting as an obstacle to kinesin and allowing kinesin to efficiently navigate the microtubule surface (Stern *et al.*, 2017).

The variation in responses of different cargoes to tau is likely determined by the types of kinesin motors driving their movement. While characterization of the set of motor proteins and adaptors that transport different cargoes is ongoing, current evidence suggests that kinesins-1, -2, and -3 contribute to early endosome and lysosome motility but that the relative stoichiometry and activity of
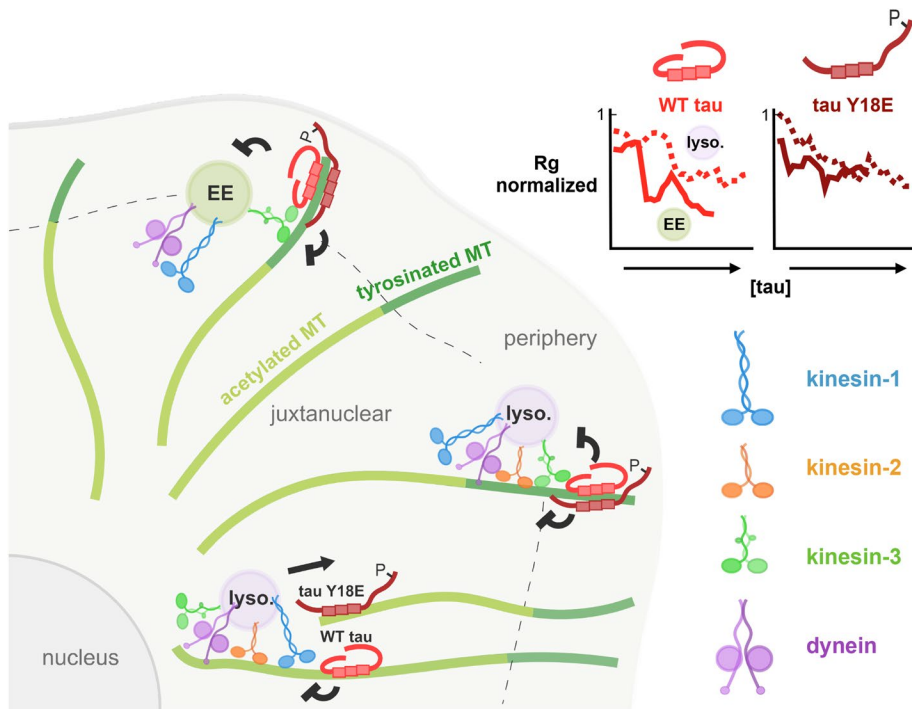
FIGURE 7: Model for the regulation of vesicle transport by tau Y18 phosphorylation. Kinesin-1–driven lysosome (lyso.) transport is inhibited by WT tau but is less sensitive to phosphomimetic tau. Kinesin-3–driven transport of early endosomes (EE) and peripheral lysosomes is inhibited by both WT and phosphomimetic tau. The Rg (normalized to control) of early endosomes shows a steeper decrease with increasing tau levels in cells, indicating that early endosome motility is more sensitive to tau inhibition compared with lysosomes.

(Cai *et al.*, 2009; Norris *et al.*, 2014; Guardia *et al.*, 2016; Katrukha *et al.*, 2017; Tas *et al.*, 2017). These juxtanuclear lysosomes maintained levels of motility similar to those of control in the presence of phosphomimetic tau (Figure 3). Our live cell and in vitro observations show that modifying tau by phosphorylation modulates its effect on cargo transport and that the effect of tau phosphorylation is likely dependent on the engaged motor proteins specific to different endocytic cargoes (Figure 7).

Kinesin-3 (KIF1A) interacts with the tubulin C-terminal tails, which prolongs its contact with the microtubule and causes temporary pausing of the motor protein. KIF1A can then undertake more consecutive runs following pauses (Lessard *et al.*, 2019). As tau also interacts with the C-terminal tails of tubulin, important for its diffusive behavior (Hinrichs *et al.*, 2012), kinesin-3 and tau might compete for the same binding sites on the microtubule (Lessard *et al.*, 2019) (Figure 6C). Our results indicate that phosphomimetic tau at Y18 is more inhibitory to KIF1A in vitro than WT tau, possibly because the higher diffusivity of phosphomimetic tau (Stern *et al.*, 2017) increases its potential occupancy of more tubulin C-terminal tails over a wider microtubule surface. In turn, this decreases the pausing behavior of kinesin-3 due to limited access to tubulin C-terminal tails, and thus its overall run lengths are reduced over long distances. In contrast, kinesin-1 is relatively insensitive to tubulin posttranslational modifications like polyglutamylation that alter the C-terminal tails (Sirajuddin *et al.*, 2014), further supporting a putative role for C-terminal tubulin tails in mediating the inhibition of kinesin-3 by phophomimetic tau.

The cell directs cargo transport by dynamically modulating interactions between MAPs and the microtubule surface by posttranslational modifications of microtubules and MAPs, based on cellular functions and development. For example, the proximo-distal gradient of tau phosphorylation states changes during neuronal differentiation, with differing levels of tau phosphorylation in the soma and proximal axon compared with the axonal growth cone (Mandell and Banker, 1996). Future work investigating the roles of tau phosphorylation in neurons (Supplemental Figure S8) will elucidate the regulatory effects of tau on intracellular transport. Our results indicate that tau phosphorylation impacts specific cargoes at specific subcellular localizations. Accordingly, aberrant tau phosphorylation would be expected to disrupt the targeting of organelles to their specific destinations in the cell.

MATERIALS AND METHODS
Request a protocol through *Bio-protocol*.

DNA constructs
Tau-mApple, consisting of the human 3RS-tau sequence, the shortest isoform expressed in the CNS (confirmed by BLAST alignment), fused at the C-terminus to mApple, was a gift from Michael Davidson (Florida State University; mApple-MAPTau-N-10; Addgene plasmid #54925). Using the QuikChange II XL Site-Directed Mutagenesis kit

these kinesins vary among different cargoes (Beaudet *et al.*, 2022). Kinesin-2 (KIF3A/B) is the primary anterograde motor for lysosomes (Brown *et al.*, 2005). The more persistent motility of lysosomes on tau-decorated microtubules (Figure 7) relative to early endosome motility might be explained by the typically greater processivity of lysosomes in normal conditions and the presence of kinesin-2, which is less sensitive to tau compared with kinesin-1 and kinesin-3 (Figure 5D). Kinesin-2 has a longer and more flexible neck linker, which may help it circumvent tau molecules on the microtubule surface (Vershinin *et al.*, 2007; Dixit *et al.*, 2008; Hoeprich *et al.*, 2014; Chaudhary *et al.*, 2018; Monroy *et al.*, 2020). Dynein motility is largely insensitive to tau (Dixit *et al.*, 2008; Vershinin *et al.*, 2008; Chaudhary *et al.*, 2018), and we also found that retrograde motility of lysosomes is not inhibited by tau (Figure 3D). For bidirectional cargoes driven by both kinesins and dyneins, tau reduces the number of engaged kinesins, biasing movement to the microtubule minus end (Chaudhary *et al.*, 2018). In agreement, tau increases the fraction of inward-directed motility of lysosomes (Figure 1, D and E), resulting in clustering of the stationary lysosomes near the cell center (Figure 1A; Supplemental Figure S6D).

When phosphomimetic mutations are made to tau (Y18E), inhibition of kinesin-1 is relieved in vitro (Stern *et al.*, 2017), while kinesin-3 is more strongly inhibited (Figure 5). In support of the motors specific to each cargo mediating differential regulation by tau, peripheral lysosomes and early endosomes are driven by kinesin-3 (Matsushita *et al.*, 2004; Lenz *et al.*, 2006; Bentley *et al.*, 2015; Guardia *et al.*, 2016). We observe that these cargoes are strongly inhibited by WT tau and more so by phosphomimetic tau (Figures 3 and 4). In contrast, lysosomes closer to the nucleus are expected to be localized on acetylated microtubules and driven by kinesin-1

(Agilent, Wilmington, DE), we generated the phosphomimetic Y18E of this tau construct by changing the plasmid's nucleotide sequence coding the amino acid at position 18 from TAC to GAA, from tyrosine (Y) to glutamic acid (E). We confirmed the nucleotide changes with Sanger sequencing using the standard CMV-F primer at the McGill University and Genome Quebec Innovation Centre (Montreal, QC). The primers (Invitrogen) designed and used for the site-directed mutagenesis are the following: 5'-CTGTCCCCCAACCCTTCCGT-CCCAGCGTG-3' and 5'-CACGCTGGGACGGAAGGGTTGGGGGA-CAG-3'. pRK5 c-Fyn, consisting of the human brain isoform B of fyn (confirmed by BLAST alignment), was a gift from Filippo Giancotti (Columbia University; Addgene plasmid #16032) (Mariotti et al., 2001). KIF1A(1-393)-LZ-3xmCitrine motors were a gift from Kristen Verhey, University of Michigan, Ann Arbor, MI. DNA plasmids were purified using anion-exchange gravity flow chromatography (Qiagen, Hilden, Germany).

Cell culture and transfection

COS-7 simian kidney fibroblast cells (American Type Culture Collection, Manassas, VA) were passaged with 0.25% trypsin-EDTA (Life Technologies, Thermo Fisher Scientific, Waltham, MA) and cultured in MatTek glass-bottom dishes (No. 1.0 Coverslip) (MatTek Corporation, Ashland, MA) in DMEM (Life Technologies) supplemented with 10% (vol/vol) fetal bovine serum (FBS) (Life Technologies) and 1% (vol/vol) Glutamax (Life Technologies). Cells were incubated at 37°C with 5% CO_2 for 24 h before transfection. Cells were then transfected with 400 ng of DNA plasmid prepared in OPTI-MEM Reduced Serum (Life Technologies), using Lipofectamine LTX with Plus-Reagent, according to the manufacturer's instructions (Invitrogen, Thermo Fisher Scientific). The transfection media containing DNA–lipid complexes was removed from the dishes after 4 h, and the cells were incubated at 37°C with fresh complete DMEM overnight (~12 h) before imaging. For nocodazole experiments, cells were treated with 10 μM nocodazole for 15 min.

Human induced neurons were induced from iPSC line AIW002-02. The iPSCs were obtained from the C-BIGR repository and were generated from the PBMC of a control 37-yr-old male donor. Briefly, the iPSCs were cultured for about a month in STEMdiff SMADi medium (STEMCELL Technologies, Vancouver, BC) to induce the formation of neuronal progenitor cells. Once good neural progenitor cell (NPC) enrichment was achieved, cells were dissociated (Accutase Cell Dissociation Reagent) and seeded on poly-L-ornithine (PO) (10 μg/ml)/laminin (15 μg/ml)-coated glass bottom dishes (World Precision Instruments, Sarasota, FL) in BrainPhys differentiation media (STEMCELL Technologies) at about 20,000 cells per cm². One day after seeding, the cells were transfected with FuGENE HD (Promega, Madison, WI) at 2.5:1 reagent:DNA according to the manufacturer's instructions. Human induced neurons were imaged at 5–7 d in vitro in differentiation medium.

Live cell lysosome imaging

Cells were incubated with 50 nM Lysotracker Deep Red (Invitrogen) for 10 min in complete DMEM. Cells were then washed and imaged in Leibovitz's L-15 medium (no phenol red) (Life Technologies) with 10% (vol/vol) FBS at 37°C, using a custom TIRF setup built on an Eclipse Ti-E inverted microscope (Nikon, Melville, NY) attached to an EMCCD camera (iXon U897; Andor Technology, South Windsor, CT). Time-lapse movies were taken at 300 ms per frame for live cell imaging, with a 1.49 numerical aperture oil-immersion 100× objective (Nikon, Melville, NY) using argon ion Spectra Physics lasers (1 mW) (MKS Instruments, Andover, MA). The pixel size was 0.160 μm. Cells were imaged within 1 h following Lysotracker staining.

Endocytosis of Qdots and imaging

To image early endosomes, 0.02 μM streptavidin-conjugated Qdot 525 (Invitrogen) were coated with 2.4 μg/ml biotin-conjugated EGF (Invitrogen) in Qdot Incubation Buffer (50 mM borate buffer, pH 8.3, 2% bovine serum albumin [BSA] [Invitrogen]) by incubation for 30 min on ice (Zajac et al., 2013). Cells were incubated on an orbital shaker with a solution of 2.2 μl of Qdot preparation in a total of 200 μl of complete DMEM for 10 min. Cells were then washed and incubated with 1× CellMask (Invitrogen) complete DMEM solution for 5 min at 37°C. Finally, cells were washed and imaged in Leibovitz's L-15 (supplemented with 10% FBS) before 1 h postinternalization (Scott et al., 2004; Loubery et al., 2008) of Qdots (time$_0$ = start of incubation of cells with Qdots). Qdots were imaged at 37°C with the same instrumentation and parameters as for lysosomes.

Quantification of tau intensity

The expression of tau-mApple following transfection varied considerably from cell to cell. To reduce variability for data analysis and to investigate the roles of tau in a dose-dependent manner, expression levels of tau were quantified based on the intensity of tau's mApple fluorescence signal in ImageJ (National Institutes of Health, Bethesda, MD). The intensities were normalized by the background intensity (area away from the cell) in the following manner: normalized tau intensity = cell-wide tau mean intensity/background mean intensity. Experimental and imaging conditions were consistent within and across all experiments. Cells were categorized in three levels of tau expression: low, medium, and high. In all cases, tau bound the microtubule filaments. Cells with low levels of tau expression (normalized tau intensity < 5) showed tau localizing nearly exclusively on microtubules with negligible levels of unbound cytosolic tau. At medium levels of tau (5 ≤ normalized tau intensity < 10), cells exhibited moderate amounts of cytosolic tau signal, mostly excluded from the peripheral region. Finally, cells with high levels of tau (normalized tau intensity ≥ 10) showed a high presence of tau in the entire cytosol.

Retrospective staining of fyn kinase and microtubules

Following live cell imaging of lysosomes, cells were fixed with 4% (wt/vol) paraformaldehyde (Sigma-Aldrich, St. Louis, MO) for 10 min. Cells were then washed with blocking buffer: 2% (wt/vol) BSA (BioShop Canada, Burlington, ON), 0.2% (wt/vol) saponin (Sigma-Aldrich) in PBS 1× (HyClone; Cytiva, Marlborough, MA). Fyn (15) primary antibody (Santa Cruz Biotechnology, Dallas, TX) was used to retrospectively stain for fyn kinase, α-tubulin primary antibody (Sigma-Aldrich) was used for total tubulin staining, and acetyl-α-tubulin primary antibody (clone 6-11B-1; Invitrogen) was used for acetylated tubulin. Following 1 h staining with primary antibody, cells were incubated with Alexa Fluor–labeled secondary antibodies (Invitrogen) for 30 min and imaged in PBS 1× with TIRF microscopy. Control cells show punctate signal with fyn antibody, while cells overexpressing fyn show cell-wide high signal (Supplemental Figure S1A).

High-resolution tracking of cargoes

Time-lapse movies for lysosomes and early endosomes were corrected for photobleaching using the histogram matching algorithm in ImageJ (Miura et al., 2014). Organelles were tracked with Track-Mate (Tinevez et al., 2017), using the Laplacian of Gaussian filter to detect cargoes with subpixel localization and the simple linear assignment problem (LAP) tracker for generating trajectories. The tracking parameters assume a maximal velocity of cargoes of 5 μm/s.

Trajectories were imported into MATLAB (MathWorks, Natick, MA) to filter them and determine their directionality and localization (generated from polar plots), as well as their R_g and MSD. Only organelles detected in the first frame of movies and present for at least five frames were included in the analysis.

Tracking-based analysis of lysosome directionality
Lysosome trajectories (from 90 s movies) were projected on polar plots with the MTOC designated as the cell center (0, 0 x, y coordinates). Moving lysosomes ($R_g \geq 0.5$ μm) were parsed as having a net outward or inward directionality, based on the rho value of the first and last points in their trajectories. The percentages of stationary and outward- or inward-moving lysosomes are the mean of cell means with SEM.

STICS analysis of lysosome directionality
STICS correlates fluorescence intensity fluctuations of image series in space and time to measure velocities and angles of mobile molecules and complexes. STICS combines the spatial information measured by 2D spatial correlations with the time-dependent transport measured by temporal correlations. This allows us to define a spatiotemporal correlation function (CF), which is a function of the spatial lags (ξ,η) and the time lag (Δt) (Hebert *et al.*, 2005):

$$r'_{ab}\left(\xi, \eta, \Delta t\right) = \frac{1}{N-\Delta t}\sum_{t=1}^{N-\Delta t}\frac{\left\langle\delta i_a\left(x, y, t\right)\delta i_b\left(x+\xi, y+\eta, t+\Delta t\right)\right\rangle}{\left\langle i_a\right\rangle_t\left\langle i_b\right\rangle_{t+\Delta t}}$$

where N is the total number of images in the time series and r'_{ab} represents the average cross-correlation function for channels a and b, for all pairs of images separated by a time lag.

We applied STICS on lysosome movies to determine directionality of motion. The temporal region of interest (TOI) size was five frames (1.5 s), corresponding to the mean directional switching time for lysosomes. The first 30 frames were analyzed for each movie. The region of interest size was set to 16 × 16 pixels. We manually established the coordinates of the cell center and calculated the angle of movement with respect to the cell center (see Figure 1E for details) to determine the direction of lysosomes. Vector angles of 0–60° represent inward motion toward cell center, 60–120° as perpendicular motion, and 120–180° as outward motion.

Analysis of lysosomal localization
The rho value of a trajectory on polar plots is the mean distance (or mean rho) of the trajectory's points (from each time frame) from the center. The rho value was normalized to the distance from cell center to cell edge, which was estimated by measuring the cell area using the formula radius = √(cell area/π). Lysosomes were considered to be localized peripherally when normalized rho of trajectory ≥ 0.85, in the juxtanuclear region when 0.5 ≤ rho < 0.85, and in the perinuclear region when <0.5 (method used in Figure 3, B–E; Supplemental Figure S6, D–F). The percentages of lysosomes categorized based on directionality represent the mean of cell means with SEM.

Alternatively, the peripheral lysosomes were counted using the Laplacian of Gaussian filter detection algorithm of TrackMate (Tinevez *et al.*, 2017) and divided by the total number of detected lysosomes in the cell. The periphery was defined as ~6 μm from the cell edge. Following the tracing of the cell contour, the inner peripheral line was drawn using the eroding feature in ImageJ. Cells with a total area > 2000 μm² were selected for this analysis, as the perinuclear cloud of smaller cells is typically very close to the periphery (method used for Supplemental Figure S6, A and C).

Motility analysis
The radius of gyration of lysosome or early endosome trajectories (from 90 s movies) was calculated with the following equation:

$$R_g = \sqrt{\frac{1}{n}\sum_i^n\left(\left(x_i - \bar{X}\right)^2 + \left(y_i - \bar{Y}\right)^2\right)}$$

Each trajectory consists of a number n of detected spots at consecutive time frames. Here, the R_g of a trajectory represents the deviation in 2D space of the positions x_i and y_i of a time point i within the trajectory from the mean position of all spots, $\bar{X}$ and $\bar{Y}$. R_g is the average deviation from the center of mass and thus can be simply thought of as the radius of a circle that contains half of the spots of the trajectory. In other words, the R_g is a measure of the traveled distances of lysosomes or early endosomes from the center of their trajectory. Minimal thresholds for R_g were not applied when studying the motion of all lysosomes or early endosomes (Figures 2 and 4). A minimal R_g threshold of 0.5 μm was used to differentiate between stationary and moving lysosomes (Figures 1 and 3).

The MSD of particle trajectories in x and y (two dimensions) was analyzed using a package (MSDanalyzer) developed for MATLAB (Tarantino *et al.*, 2014). The first 10% of log-log transformed MSD curves over 90 s movies (for lysosomes) or 30 s movies (early endosomes) were fitted to a linear function to determine the exponent α value (Tarantino *et al.*, 2014). Fits of low quality (R^2 coefficient < 0.8) were discarded from the distribution of α values. The SEM was calculated as SEM ≈ weighted SD/√number of degrees of freedom (Tarantino *et al.*, 2014). Overall, the trends from the R_g and MSD measurements are in agreement.

Microtubule density analysis
Microtubule organization was studied by qualitatively studying the network configuration. Microtubules are typically organized radially from the MTOC, with few microtubules bending or bundling in the periphery; this type of organization was considered normal (Supplemental Figure S4E, top schematic). With higher levels of tau expression, many microtubule filaments were seen circling the periphery (Supplemental Figure S4E, left schematic) or forming dense bundles in a ring-like configuration (Supplemental Figure S4E, right schematic). In addition, the peripheral density of the microtubule network was analyzed by calculating the mean intensity of tubulin staining in the peripheral region (~6 μm from the cell edge) normalized to the mean background intensity.

SIM imaging and reconstruction
COS-7 cells were plated on FluoroDish Cell Culture Dishes (World Precision Instruments) with 0.17 mm glass coverslip thickness. Cells were transfected and prepared for imaging following the same procedure as above and imaged with an Elyra 7 wide field–based superresolution microscope (Zeiss, Jena, Germany) and pco.edge 4.2 cooled sCMOS camera (Excelitas PCO, Kelheim, Germany). An alpha plan-apochromat 63× (NA 1.46) oil objective (Zeiss) was used to image the cells in Apotome mode, with a fiber-coupled solid state laser (561 nm, 50% of 75 mW) and diode pumped solid state lasers (642 nm, 50% of 75 mW). Movies were recorded at 50 ms per frame with 15 Z-stacks at a range of 6 μm with 0.403 μm intervals between the stacks. Using Zen Black SR 3.0 software (Zeiss), the SIM reconstructions were performed, and movies were rendered as maximum Z-projections using ImageJ. 3D reconstructions were used to calculate the distance of the first point of trajectories from cell center (rho).

In vitro KIF1A motility assays

KIF1A(1–393)-LZ-3xmCitrine motors (a gift from Kristen Verhey, University of Michigan, Ann Arbor, MI) were expressed in COS-7 monkey kidney fibroblasts (American Type Culture Collection, Manassas, VA) as previously described (Lessard et al., 2019). 3RS-tau expression, mutagenesis, purification, and labeling were conducted as previously described (Stern et al., 2017). Bovine tubulin isolation and paclitaxel-stabilized, fluorescently labeled microtubule polymerization were conducted as previously described (Lessard et al., 2019). In experiments containing tau, microtubules were polymerized in the absence of labeled tubulin. Microtubules were then incubated with 200 nM Alexa 647–labeled 3RS-tau for 20 min at 37°C. After incubation, microtubules were centrifuged at room temperature for 30 min at 15,000 rpm and resuspended in motility buffer. KIF1A in vitro motility assays were conducted as previously described (Lessard et al., 2019). Of note, in vitro motility assays were conducted in a motility buffer of 12 mM PIPES, 1 mM $MgCl_2$, 1 mM EGTA (ethylene glycol-bis(β-aminoethyl)-N,N,N',N'-tetraacetic acid), supplemented with 20 µM paclitaxel, 10 mM dithiothreitol (DTT), 1 mM $MgCl_2$, 10 mg/ml BSA, 2 mM ATP and an oxygen scavenger system (5.8 mg/ml glucose, 0.045 mg/ml catalase, and 0.067 mg/ml glucose oxidase). Motility events were analyzed as previously reported (Hoeprich et al., 2014, 2017). In brief, overall run length and speed data were measured using the ImageJ (v. 2.0.0; National Institutes of Health, Bethesda, MD) MTrackJ plug-in for a frame-by-frame quantification of KIF1A motility. Run length and SD were calculated and adjusted for microtubule track length as previously reported (Thompson et al., 2013).

Tau immunostaining of iPSC-derived neurons and COS-7 cells

After ten days of terminal differentiation, iPSC-derived cortical neurons were washed with PBS 1× prewarmed at 37°C and fixed with 4% paraformaldehyde for 15 min. Coverslips were rinsed 3× with PBS 1×, permeabilized with 0.3% Triton X-100 (Sigma-Aldrich) for 5 min. and then incubated with blocking buffer (2% BSA, 0.1% Triton X-100 in PBS 1×) for 1 h at room temperature. Neurons were incubated with tau-5 (clone 5) primary antibody (Sigma-Aldrich) for 2 h and with Alexa Fluor 647–labeled secondary antibody (Invitrogen) for 45 min., following washes with blocking buffer. Coverslips were mounted on slides with ProLong Diamond Antifade Mountant (Invitrogen) and imaged with TIRF microscopy at 300 ms per frame exposure on a 100× objective (Nikon).

COS-7 cells transfected with WT tau alone or with fyn kinase were similarly stained with tau-5 (Sigma-Aldrich) or with tau-9g3 primary antibody (GeneTex, Irvine, CA) followed by Alexa Fluor 647–labeled secondary antibody (Invitrogen) at the same concentrations and incubation times as tau-5 staining of iPSC-derived neurons and imaged with the same parameters.

Statistical analysis

The sliding means of Rg and α values of lysosome or early endosome trajectories with respect to tau intensity were averaged with a bin size of five along the x-axis, using bootstrapping over 1000 iterations and with 95% CIs to determine statistical significance (Chaubet et al., 2020). The sliding means of cell data points were similarly calculated, except that the fraction of the total number of data points included in individual bins and the number of bins averaged for the means were adapted based on sample size but kept constant across conditions per analysis. The distribution of α values was analyzed using one-way ANOVA and multiple comparison post-hoc

Tukey's test for comparing control and low levels of WT tau and Y18E tau. One-way ANOVA and Tukey's test were used to determine differences between the distributions of stationary or moving lysosome percentages in the peripheral, juxtanuclear, and perinuclear regions of cells expressing low levels of WT tau and Y18E tau compared with control. The Rg of moving lysosomes (in peripheral, juxtanuclear, perinuclear regions) were log-normalized, and one-way ANOVA with Tukey's test was used to determine the p values between control and low levels of WT tau and Y18E tau conditions. We also confirmed the results with the Kruskal–Wallis nonparametric test (without log normalization). Two-way ANOVA (2 × 2 factorial design) was used to distinguish the effects of low levels of WT tau, fyn, and the interaction of WT tau with fyn on vesicle motility in cells coexpressing WT tau and fyn. For in vitro motility assays, effects on overall run lengths and overall speed between control, WT tau, and Y18E tau were determined using one-way ANOVA and post-hoc Tukey tests. All statistical tests were performed with MATLAB (MathWorks).

REFERENCES

Balabanian L, Berger CL, Hendricks AG (2017). Acetylated microtubules are preferentially bundled leading to enhanced kinesin-1 motility. Biophys J 113, 1551–1560.

Balabanian L, Chaudhary AR, Hendricks AG (2018). Traffic control inside the cell: microtubule-based regulation of cargo transport. Biochem 40, 14–17.

Ballatore C, Lee VM, Trojanowski JQ (2007). Tau-mediated neurodegeneration in Alzheimer's disease and related disorders. Nat Rev Neurosci 8, 663–672.

Beaudet D, Berger CL, Hendricks AG (2022). Tau inhibits the long-range, dynein-mediated motility of early phagosomes. bioRxiv, 495679.

Bentley M, Decker H, Luisi J, Banker G (2015). A novel assay reveals preferential binding between Rabs, kinesins, and specific endosomal subpopulations. J Cell Biol 208, 273–281.

Black MM, Slaughter T, Moshiach S, Obrocka M, Fischer I (1996). Tau is enriched on dynamic microtubules in the distal region of growing axons. J Neurosci 16, 3601–3619.

Blatner NR, Wilson MI, Lei C, Hong W, Murray D, Williams RL, Cho W (2007). The structural basis of novel endosome anchoring activity of KIF16B kinesin. EMBO J 26, 3709–3719.

Brown CL, Maier KC, Stauber T, Ginkel LM, Wordeman L, Vernos I, Schroer TA (2005). Kinesin-2 is a motor for late endosomes and lysosomes. Traffic 6, 1114–1124.

Cai D, McEwen DP, Martens JR, Meyhofer E, Verhey KJ (2009). Single molecule imaging reveals differences in microtubule track selection between kinesin motors. PLoS Biol 7, e1000216.

Chaubet L, Chaudhary AR, Heris HK, Ehrlicher AJ, Hendricks AG (2020). Dynamic actin cross-linking governs the cytoplasm's transition to fluid-like behavior. Mol Biol Cell 31, 1744–1752.

Chaudhary AR, Berger F, Berger CL, Hendricks AG (2018). Tau directs intracellular trafficking by regulating the forces exerted by kinesin and dynein teams. Traffic 19, 111–121.

Chen J, Kanai Y, Cowan NJ, Hirokawa N (1992). Projection domains of MAP2 and tau determine spacings between microtubules in dendrites and axons. Nature 360, 674–677.

Delevoye C, Miserey-Lenkei S, Montagnac G, Gilles-Marsens F, Paul-Gilloteaux P, Giordano F, Waharte F, Marks MS, Goud B, Raposo G (2014). Recycling endosome tubule morphogenesis from sorting endosomes requires the kinesin motor KIF13A. Cell Rep 6, 445–454.

Dixit R, Ross JL, Goldman YE, Holzbaur EL (2008). Differential regulation of dynein and kinesin motor proteins by tau. Science 319, 1086–1089.

Ghiretti AE, Thies E, Tokito MK, Lin T, Ostap EM, Kneussel M, Holzbaur ELF (2016). Activity-dependent regulation of distinct transport and cytoskeletal remodeling functions of the dendritic kinesin KIF21B. Neuron 92, 857–872.

Guardia CM, Farias GG, Jia R, Pu J, Bonifacino JS (2016). BORC functions upstream of kinesins 1 and 3 to coordinate regional movement of lysosomes along different microtubule tracks. Cell Rep 17, 1950–1961.

Guedes-Dias P, Nirschl JJ, Abreu N, Tokito MK, Janke C, Magiera MM, Holzbaur ELF (2019). Kinesin-3 responds to local microtubule dynamics to target synaptic cargo delivery to the presynapse. Curr Biol 29, 268–282.e268.

Guzik-Lendrum S, Rank KC, Bensel BM, Taylor KC, Rayment I, Gilbert SP (2015). Kinesin-2 KIF3AC and KIF3AB can drive long-range transport along microtubules. Biophys J 109, 1472–1482.

Hammond JW, Cai D, Blasius TL, Li Z, Jiang Y, Jih GT, Meyhofer E, Verhey KJ (2009). Mammalian kinesin-3 motors are dimeric in vivo and move by processive motility upon release of autoinhibition. PLoS Biol 7, e72.

Hancock WO (2014). Bidirectional cargo transport: moving beyond tug of war. Nat Rev Mol Cell Biol 15, 615–628.

Hebert B, Costantino S, Wiseman PW (2005). Spatiotemporal image correlation spectroscopy (STICS) theory, verification, and application to protein velocity mapping in living CHO cells. Biophys J 88, 3601–3614.

Hinrichs MH, Jalal A, Brenner B, Mandelkow E, Kumar S, Scholz T (2012). Tau protein diffuses along the microtubule lattice. J Biol Chem 287, 38559–38568.

Hirokawa N, Takemura R (2005). Molecular motors and mechanisms of directional transport in neurons. Nat Rev Neurosci 6, 201–214.

Hoepfner S, Severin F, Cabezas A, Habermann B, Runge A, Gillooly D, Stenmark H, Zerial M (2005). Modulation of receptor recycling and degradation by the endosomal kinesin KIF16B. Cell 121, 437–450.

Hoeprich GJ, Mickolajczyk KJ, Nelson SR, Hancock WO, Berger CL (2017). The axonal transport motor kinesin-2 navigates microtubule obstacles via protofilament switching. Traffic 18, 304–314.

Hoeprich GJ, Thompson AR, McVicker DP, Hancock WO, Berger CL (2014). Kinesin's neck-linker determines its ability to navigate obstacles on the microtubule surface. Biophys J 106, 1691–1700.

Janke C (2014). The tubulin code: molecular components, readout mechanisms, and functions. J Cell Biol 206, 461–472.

Kanaan NM, Morfini G, Pigino G, LaPointe NE, Andreadis A, Song Y, Leitman E, Binder LI, Brady ST (2012). Phosphorylation in the amino terminus of tau prevents inhibition of anterograde axonal transport. Neurobiol Aging 33, 826.e15–30.

Kanaan NM, Morfini GA, LaPointe NE, Pigino GF, Patterson KR, Song Y, Andreadis A, Fu Y, Brady ST, Binder LI (2011). Pathogenic forms of tau inhibit kinesin-dependent axonal transport through a mechanism involving activation of axonal phosphotransferases. J Neurosci 31, 9858–9868.

Kanai Y, Chen J, Hirokawa N (1992). Microtubule bundling by tau proteins in vivo: analysis of functional domains. EMBO J 11, 3953–3961.

Kanai Y, Hirokawa N (1995). Sorting mechanisms of tau and MAP2 in neurons: suppressed axonal transit of MAP2 and locally regulated microtubule binding. Neuron 14, 421–432.

Katrukha EA, Mikhaylova M, van Brakel HX, van Bergen En Henegouwen PM, Akhmanova A, Hoogenraad CC, Kapitein LC (2017). Probing cytoskeletal modulation of passive and active intracellular dynamics using nanobody-functionalized quantum dots. Nat Commun 8, 14772.

Klein C, Kramer EM, Cardine AM, Schraven B, Brandt R, Trotter J (2002). Process outgrowth of oligodendrocytes is promoted by interaction of fyn kinase with the cytoskeletal protein tau. J Neurosci 22, 698–707.

Konishi Y, Setou M (2009). Tubulin tyrosination navigates the kinesin-1 motor domain to axons. Nat Neurosci 12, 559–567.

Kosik KS, Finch EA (1987). MAP2 and tau segregate into dendritic and axonal domains after the elaboration of morphologically distinct neurites: an immunocytochemical study of cultured rat cerebrum. J Neurosci 7, 3142–3153.

LaPointe NE, Morfini G, Pigino G, Gaisina IN, Kozikowski AP, Binder LI, Brady ST (2009). The amino terminus of tau inhibits kinesin-dependent axonal transport: implications for filament toxicity. J Neurosci Res 87, 440–451.

Lee G, Thangavel R, Sharma VM, Litersky JM, Bhaskar K, Fang SM, Do LH, Andreadis A, Van Hoesen G, Ksiezak-Reding H (2004). Phosphorylation of tau by fyn: implications for Alzheimer's disease. J Neurosci 24, 2304–2312.

Lenz JH, Schuchardt I, Straube A, Steinberg G (2006). A dynein loading zone for retrograde endosome motility at microtubule plus-ends. EMBO J 25, 2275–2286.

Lessard DV, Zinder OJ, Hotta T, Verhey KJ, Ohi R, Berger CL (2019). Polyglutamylation of tubulin's C-terminal tail controls pausing and motility of kinesin-3 family member KIF1A. J Biol Chem 294, 6353–6363.

Loubery S, Wilhelm C, Hurbain I, Neveu S, Louvard D, Coudrier E (2008). Different microtubule motors move early and late endocytic compartments. Traffic 9, 492–509.

Malaby HL, Lessard DV, Berger CL, Stumpff J (2019). KIF18A's neck linker permits navigation of microtubule-bound obstacles within the mitotic spindle. Life Sci Alliance 2, e201800169.

Mandell JW, Banker GA (1996). A spatial gradient of tau protein phosphorylation in nascent axons. J Neurosci 16, 5727–5740.

Mariotti A, Kedeshian PA, Dans M, Curatola AM, Gagnoux-Palacios L, Giancotti FG (2001). EGF-R signaling through Fyn kinase disrupts the function of integrin alpha6beta4 at hemidesmosomes: role in epithelial cell migration and carcinoma invasion. J Cell Biol 155, 447–458.

Matsushita M, Tanaka S, Nakamura N, Inoue H, Kanazawa H (2004). A novel kinesin-like protein, KIF1Bbeta3 is involved in the movement of lysosomes to the cell periphery in non-neuronal cells. Traffic 5, 140–151.

McVicker DP, Chrin LR, Berger CL (2011). The nucleotide-binding state of microtubules modulates kinesin processivity and the ability of Tau to inhibit kinesin-mediated transport. J Biol Chem 286, 42873–42880.

McVicker DP, Hoeprich GJ, Thompson AR, Berger CL (2014). Tau interconverts between diffusive and stable populations on the microtubule surface in an isoform and lattice specific manner. Cytoskeleton 71, 184–194.

Miura K, Rietdorf J, Rueden CT, Schindelin JE, Hiner MC (2014). ImageJ Plugin CorrectBleach V2.0.2.

Monroy BY, Sawyer DL, Ackermann BE, Borden MM, Tan TC, Ori-McKenney KM (2018). Competition between microtubule-associated proteins directs motor transport. Nat Commun 9, 1487.

Monroy BY, Tan TC, Oclaman JM, Han JS, Simó S, Niwa S, Nowakowski DW, McKenney RJ, Ori-McKenney KM (2020). A combinatorial MAP code dictates polarized microtubule transport. Dev Cell 53, 60–72.e64.

Morfini G, Szebenyi G, Brown H, Pant HC, Pigino G, DeBoer S, Beffert U, Brady ST (2004). A novel CDK5-dependent pathway for regulating GSK3 activity and kinesin-driven motility in neurons. EMBO J 23, 2235–2245.

Norris SR, Soppina V, Dizaji AS, Schimert KI, Sept D, Cai D, Sivaramakrishnan S, Verhey KJ (2014). A method for multiprotein assembly in cells reveals independent action of kinesins in complex. J Cell Biol 207, 393–406.

Pu J, Guardia CM, Keren-Kaplan T, Bonifacino JS (2016). Mechanisms and functions of lysosome positioning. J Cell Sci 129, 4329–4339.

Rodriguez-Martin T, Cuchillo-Ibanez I, Noble W, Nyenya F, Anderton BH, Hanger DP (2013). Tau phosphorylation affects its axonal transport and degradation. Neurobiol Aging 34, 2146–2157.

Samsonov A, Yu JZ, Rasenick M, Popov SV (2004). Tau interaction with microtubules in vivo. J Cell Sci 117, 6129–6141.

Scott CW, Klika AB, Lo MM, Norris TE, Caputo CB (1992). Tau protein induces bundling of microtubules in vitro: comparison of different tau isoforms and a tau protein fragment. J Neurosci Res 33, 19–29.

Scott DB, Michailidis I, Mu Y, Logothetis D, Ehlers MD (2004). Endocytosis and degradative sorting of NMDA receptors by conserved membrane-proximal signals. J Neurosci 24, 7096–7109.

Sergeant N, Bretteville A, Hamdane M, Caillet-Boudin M-L, Grognet P, Bombois S, Blum D, Delacourte A, Pasquier F, Vanmechelen E, et al. (2008). Biochemistry of Tau in Alzheimer's disease and related neurological disorders. Expert Rev Proteomics 5, 207–224.

Serra-Marques A, Martin M, Katrukha EA, Grigoriev I, Peeters CA, Liu Q, Hooikaas PJ, Yao Y, Solianova V, Smal I, et al. (2020). Concerted action of kinesins KIF5B and KIF13B promotes efficient secretory vesicle transport to microtubule plus ends. eLife 9, e61302.

Shastry S, Hancock WO (2011). Interhead tension determines processivity across diverse N-terminal kinesins. Proc Natl Acad Sci USA 108, 16253–16258.

Sirajuddin M, Rice LM, Vale RD (2014). Regulation of microtubule motors by tubulin isotypes and post-translational modifications. Nat Cell Biol 16, 335–344.

Stern JL, Lessard DV, Hoeprich GJ, Morfini GA, Berger CL (2017). Phospho-regulation of Tau modulates inhibition of kinesin-1 motility. Mol Biol Cell 28, 1079–1087.

Takemura R, Okabe S, Umeyama T, Kanai Y, Cowan NJ, Hirokawa N (1992). Increased microtubule stability and alpha tubulin acetylation in cells transfected with microtubule-associated proteins MAP1B, MAP2 or tau. J Cell Sci 103(Pt 4), 953–964.

Tarantino N, Tinevez JY, Crowell EF, Boisson B, Henriques R, Mhlanga M, Agou F, Israel A, Laplantine E (2014). TNF and IL-1 exhibit distinct ubiquitin requirements for inducing NEMO-IKK supramolecular structures. J Cell Biol 204, 231–245.

Tarhan MC, Orazov Y, Yokokawa R, Karsten SL, Fujita H (2013). Biosensing MAPs as "roadblocks": kinesin-based functional analysis of tau protein isoforms and mutants using suspended microtubules (sMTs). Lab Chip 13, 3217–3224.

Tas RP, Chazeau A, Cloin BMC, Lambers MLA, Hoogenraad CC, Kapitein LC (2017). Differentiation between oppositely oriented microtubules controls polarized neuronal transport. Neuron 96, 1264–1271.e5.

Thompson AR, Hoeprich GJ, Berger CL (2013). Single-molecule motility: statistical analysis and the effects of track length on quantification of processive motion. Biophys J 104, 2651–2661.

Tinevez JY, Perry N, Schindelin J, Hoopes GM, Reynolds GD, Laplantine E, Bednarek SY, Shorte SL, Eliceiri KW (2017). TrackMate: an open and extensible platform for single-particle tracking. Methods 115, 80–90.

Verhey KJ, Gaertig J (2007). The tubulin code. Cell Cycle 6, 2152–2160.

Vershinin M, Carter BC, Razafsky DS, King SJ, Gross SP (2007). Multiple-motor based transport and its regulation by Tau. Proc Natl Acad Sci USA 104, 87–92.

Vershinin M, Xu J, Razafsky DS, King SJ, Gross SP (2008). Tuning microtubule-based transport through filamentous MAPs: the problem of dynein. Traffic 9, 882–892.

White R, Kramer-Albers EM (2014). Axon-glia interaction and membrane traffic in myelin formation. Front Cell Neurosci 7, 284.

Xia D, Gutmann JM, Götz J (2016). Mobility and subcellular localization of endogenous, gene-edited Tau differs from that of over-expressed human wild-type and P301L mutant Tau. Sci Rep 6, 29074.

Yu D, Feinstein SC, Valentine MT (2016). Effects of wild type tau and disease-linked tau mutations on microtubule organization and intracellular trafficking. J Biomech 49, 1280–1285.

Zajac AL, Goldman YE, Holzbaur EL, Ostap EM (2013). Local cytoskeletal and organelle interactions impact molecular-motor-driven early endosomal trafficking. Curr Biol 23, 1173–1180.